

# Mid-infrared imaging of active galaxies

## Active nuclei and embedded star clusters

E. Galliano<sup>1</sup>, D. Alloin<sup>1,2</sup>, E. Pantin<sup>2</sup>, P. O. Lagage<sup>2</sup>, and O. Marco<sup>1</sup>

<sup>1</sup> European Southern Observatory, Casilla 19001, Santiago 19, Chile  
e-mail: egallian@eso.org

<sup>2</sup> UMR7158 CEA-CNRS-U.Paris7, DSM/DAPNIA/Service d'Astrophysique, CEA/Saclay, 91191 Gif-sur-Yvette, France

Received 11 March 2005 / Accepted 5 April 2005

**Abstract.** High resolution, mid-infrared (MIR) images of nine nearby active galaxies are presented. The data were obtained with the TIMMI 2 instrument mounted at the ESO 3.6 m telescope using a set of  $N$ -band narrow filters. The resulting images have an angular resolution of  $0.6''$ – $1''$ . The MIR emission has been resolved in four galaxies: NGC 253, NGC 1365, NGC 1808 and NGC 7469. The images show a circumnuclear population of unknown MIR sources in NGC 1365 and NGC 1808, coincident with radio sources. These MIR/radio sources are interpreted in terms of embedded young star clusters. A high-resolution MIR map of NGC 253 is also presented, and enables the identification of a previously unknown MIR counterpart to the radio nucleus. Extended MIR emission is detected in NGC 7469, and concurs with previous observations in the NIR and radio. For this source, an interesting morphological difference between the  $10.4\ \mu\text{m}$  and the  $11.9\ \mu\text{m}$  emission is observed, suggesting the presence of a dust-rich micro-bar. Our MIR images of Circinus do not show resolved emission from the nucleus down to an angular scale of  $0.5''$ . In the case of NGC 2992, an upper limit to the extended MIR emission can be set. We provide new MIR flux measurements for the unresolved AGN in NGC 5995, IZw1 and IIZw136.

**Key words.** galaxies: individual: NGC 253 – galaxies: individual: NGC 1808 – galaxies: individual: NGC 1365 – galaxies: star clusters – infrared: galaxies – galaxies: Seyfert

### 1. Introduction

As mid-infrared (MIR) radiation is much less affected by extinction than visible light, dust embedded objects in the nuclear regions of galaxies are more efficiently detected in this wavelength range. High spatial resolution in the MIR requires the use of large-aperture telescopes and thus is restricted to ground-based instruments that provide a substantial gain in spatial resolution over currently available MIR instruments in space. The gain in spatial resolution is, in the context of active galaxies, essential since in many cases the relative contributions to their total power of the starburst activity and of the active galactic nucleus (AGN) are unknown. Let us briefly discuss how high resolution MIR observations can help probe/disentangle these two phenomena.

Young bursts of star formation are likely to be substantially obscured by dust. Therefore, high resolution MIR imaging is an appropriate means of identifying them. Indeed, recent infrared (IR) observations have revealed the existence of very bright embedded star clusters, containing a few thousand O stars, which are invisible on images obtained in the optical. The first object of this type to be discovered was the deeply buried star cluster in the Antennae galaxy by Mirabel et al. (1998). It produces 20% of the total MIR emission of the galaxy, and

contains  $1.6 \times 10^7 M_{\odot}$  of stars hidden behind an  $A_V = 10$  cloud of dust (Gilbert et al. 2000). Similar objects have been found in NGC 5253 (Gorjian et al. 2001), SBS 0335-052 (Plante & Sauvage 2002) and IIZw40 (Beck et al. 2002).

High resolution MIR imaging is also essential for the identification and classification of AGN. For sources affected by intrinsically large extinction, an optically-based classification can be quite misleading. For example, Krabbe et al. (2001) noted that the classification of “active galaxies” based solely upon their optical properties is a poor indicator since X-ray or radio observations could reveal the presence of an AGN in “classical” starburst galaxies. Conversely, ISO observations (Laurent 1999) of optically classified AGN show that their MIR emission is often dominated by star forming regions rather than by the AGN itself. Thus by spatially resolving emission from star forming regions and AGN, and photometrically measuring each through high resolution imaging, one can determine their relative contributions to the total integrated power. For AGN, precise and spatially resolved MIR photometry is mandatory in order to construct spectral energy distributions (SED) that are free of starburst contributions. The resultant SED may then be compared to models developed in the framework of the unified scheme. Due to the intrinsic small size of the dusty torus in AGN (1 to a few  $\times 100$  pc), only a few can be directly probed

through a spatially resolved mapping of their MIR emission. One of these is the extensively studied type 2 AGN in NGC 1068. MIR imaging of this source at  $0.6''$  resolution revealed extended and collimated 10 and  $20\ \mu\text{m}$  emission up to  $5''$  from the core, along the direction of the radio jet (Alloin et al. 2000). At higher angular resolution ( $0.1''$  after deconvolution: Bock et al. 2000; Tomono et al. 2001), the complex structure of the MIR emission is found to be coincident with the narrow line region (NLR) clouds (Galliano et al. 2003). Therefore, the access to high resolution imaging brings new clues regarding the morphology of the material around the central engines of AGN.

This paper presents high angular resolution MIR images of a sample of active galaxies, obtained with the TIMMI 2 instrument at the ESO 3.6 m telescope, La Silla observatory. Observations and data reduction are presented and discussed in Sect. 2 and the results are given in Sect. 3. First, the general results such as flux measurements and maps for the resolved objects are given in Sect. 3.1. Then, we provide more detailed analyses for NGC 253 (Sect. 3.2), Circinus (Sect. 3.3), NGC 1808 (Sect. 3.4), NGC 1365 (Sect. 3.5) and NGC 7469 (Sect. 3.6). Section 4 presents high spatial resolution IR flux measurements and provides SED for the targets. We discuss in Sect. 5 the newly discovered populations of MIR sources in NGC 1808 and NGC 1365: a simple model supports the interpretation in terms of embedded star clusters. A detailed discussion of these sources will be presented along with new observations in a forthcoming paper. A summary and conclusions are given in Sect. 6. A Hubble constant  $H_0 = 75\ \text{km s}^{-1}\ \text{Mpc}^{-1}$  is used throughout the article to compute the distance to the objects, except when measured with a more precise method.

## 2. Observations, data reduction and templates

### 2.1. Observations

The original aims of this study were two-fold: (1) perform preliminary observations of active galaxies in order to prepare future observations with VISIR at the VLT, (2) look for extended MIR emission directly related to the AGN, as was observed along the radio jet direction in NGC 1068 (Alloin et al. 2000; Bock et al. 2000; Tomono et al. 2001). To address these aims, we chose a sample of nearby (few Mpc) to moderately nearby (few hundreds of Mpc) AGN. The observations quickly showed interesting by-products such as the star forming environment around some AGN: the MIR counterparts of known radio sources in NGC 1365 and NGC 1808 were revealed. After these first findings, we decided to include in our sample NGC 253, the archetypal starburst galaxy. Table 1 displays basic information about the targets.

The observations were performed with TIMMI 2 (Thermal Infrared Multi Mode Instrument<sup>1</sup>) installed at the 3.6 m telescope on La Silla during four runs, on 2001 March 10–11, July 5, October 8 and November 26. TIMMI 2 is equipped with

a  $240 \times 320$  pixel AsSi BIB detector and we observed with an  $0.2''$  pixel size, resulting in a field of view of  $48'' \times 64''$ .

Four narrow filters spanning the *N*-band were available: the  $8.9\ \mu\text{m}$  filter ( $7.90\text{--}9.46\ \mu\text{m}$ ), the  $10.4\ \mu\text{m}$  filter ( $9.46\text{--}11.21\ \mu\text{m}$ ), the  $11.9\ \mu\text{m}$  filter ( $10.61\text{--}12.50\ \mu\text{m}$ ) and the  $12.9\ \mu\text{m}$  filter ( $11.54\text{--}12.98\ \mu\text{m}$ ). The labels of the filters do not correspond to their effective wavelengths, but rather refer to the spectral features they probe. One filter is also available in the *Q*-band ( $20\ \mu\text{m}$ ). The seeing was good,  $\sim 0.6\text{--}1.0''$  in the visible and allowed us to obtain diffraction-limited images at all observed MIR wavelengths. The main difficulties in performing MIR observations from the ground are the high level of sky emission and the variability of the sky transparency, particularly in the  $20\ \mu\text{m}$  window.

### 2.2. Data reduction

The standard chopping/nodding technique was used to determine the sky and telescope background for subtraction. We observed in “small imaging mode”, which means that the nodding direction was perpendicular to the chopping direction. On-line reduction at the telescope allowed the chopping throws and nodding offsets to be adjusted depending on the extension of the sources. Chopping throws between  $15''$  and  $20''$  and nodding offsets from  $15''$  to  $30''$  were used. MIR standard stars were observed before and after each source observation in order to calibrate the photometry of the final images, evaluate variations of the sky transparency, and estimate the Point Spread Functions (PSF) for further image deconvolution. IDL routines were written and used for data reduction. Glitches were carefully removed and the data were corrected for the TIMMI 2 bias: each of the sixteen readout channels of the chip has a response which varies with time. This appears on the images as sixteen vertical bands with slightly different intensity levels. This detector feature makes the flat field correction useless, as it assumes a stable detector response, at least over the time scale of an observing night. These reduction steps were performed on each plane of the data-cubes, each of these planes corresponding to the subtraction of two consecutively chopped images. Eventually, the planes of each reduced data-cube were co-added resulting in the scientifically exploitable image.

Where resolved structures were present, we deconvolved the images in order to better separate the different sources. Deconvolution was performed using the `mr_deconv` routine of the MR/1 software package developed by Murtagh & Starck (1999). Standard stars were used to determine the PSF. The MR/1 software package performs an efficient regularisation in the wavelet space. This procedure is excellent at pulling low signal out of noise, clarifying the distribution of sources. The results obtained after deconvolution were suitable for comparison with high resolution cm radio images and we could indeed clearly identify MIR counterparts for a number of radio sources. For low brightness sources within the resolved structures, we measured the fluxes on the deconvolved images. The precision of this procedure was tested with the following simulation: an artificial MIR image of NGC 1808 was created, in which weak point sources were given the fluxes measured

<sup>1</sup> <http://www.ls.eso.org/lasilla/Telescopes/360cat/timmi/>

**Table 1.** General properties of the sample galaxies: coordinates, distance, AGN type, IR flux.

| Galaxy                | RA<br>(J2000)                                     | Dec<br>(J2000) | Dist.<br>Mpc | Scale<br>pc/arcsec | Activity         | IRAS 12 $\mu\text{m}$ flux <sup>c</sup><br>Jy |
|-----------------------|---|----------------|--------------|--------------------|------------------|---|
| NGC 253 <sup>a</sup>  | 00 <sup>h</sup> 47 <sup>m</sup> 33.1 <sup>s</sup> | -25°17'18"     | 2.5          | 12                 | Starburst + AGN? | 24.0  |
| Circinus              | 14 <sup>h</sup> 13 <sup>m</sup> 09.3 <sup>s</sup> | -65°20'21"     | 4.0          | 19                 | Type 2 AGN       | 18.8  |
| NGC 1808 <sup>b</sup> | 05 <sup>h</sup> 07 <sup>m</sup> 42.3 <sup>s</sup> | -37°30'46"     | 10.9         | 53                 | Starburst + AGN? | 4.4   |
| NGC 1365              | 03 <sup>h</sup> 33 <sup>m</sup> 36.4 <sup>s</sup> | -36°08'25"     | 18.6         | 90                 | Type 2 AGN       | 3.4   |
| NGC 2992              | 21 <sup>h</sup> 32 <sup>m</sup> 27.8 <sup>s</sup> | +10°08'19"     | 30.1         | 150                | Type 2 AGN       | –   |
| NGC 7469              | 23 <sup>h</sup> 03 <sup>m</sup> 15.6 <sup>s</sup> | +08°52'26"     | 66           | 320                | Type 1 AGN       | 1.35  |
| NGC 5995              | 15 <sup>h</sup> 48 <sup>m</sup> 24.9 <sup>s</sup> | -13°45'28"     | 100          | 490                | Type 2 AGN       | 0.39  |
| IZw1                  | 00 <sup>h</sup> 53 <sup>m</sup> 34.9 <sup>s</sup> | +12°41'36"     | 245          | 1186               | Type 1 AGN       | 0.51  |
| IIZw136               | 21 <sup>h</sup> 32 <sup>m</sup> 27.8 <sup>s</sup> | +10°08'19"     | 252          | 1222               | Type 1 AGN       | <0.2  |

<sup>a</sup> A discussion about the nature of the radio nucleus of NGC 253 can be found in Forbes et al. (2000).

<sup>b</sup> The AGN nature of the nucleus of NGC 1808 is not clearly established, see the discussion in Krabbe et al. (2001) and in Sect. 4.

<sup>c</sup> Flux of the entire galaxy, from Moshir & et al. (1990).

on the deconvolved image. Poisson noise corresponding to the high background level was added. Then, this artificial image was deconvolved: after deconvolution, the input fluxes were recovered with an accuracy better than 10%. The brightest among the weak sources were all recovered, while a few false very weak sources appeared on the deconvolved image, but could be easily identified and excluded since they were more compact than real sources.

### 2.3. Photometric error estimation

The uncertainty on the flux measurements is dominated by variations of the sky transparency. In the 10  $\mu\text{m}$  window, variations of the photometric calibration (ADU to flux) during the night were found to be of about 10%. One extreme case of transparency variation occurred on 2001 November 26: the photometric calibration varied by 50% in about 20 min probably because of spatial variations of the sky transparency. This happened during the observing sequence for NGC 1365 through the 12.9  $\mu\text{m}$  filter. The corresponding data-cube was checked: we split it into equal slices, for each of which the source fluxes were measured and found to be equal. This ensured that the sky transparency had not changed dramatically while performing the science observation, but rather differed between the two standard star observations. Unfortunately, there is no way to check the spatial variation of the sky transparency. Thus, the 12.9  $\mu\text{m}$  flux measured for NGC 1365 is uncertain. Also, the values for the standard star fluxes are known to a precision that is not better than 10%. We adopt a formal error of  $\pm 20\%$  on the quoted flux measurements.

### 2.4. Templates for MIR sources: AGN, HII region and PDR

The MIR emission observed in galaxies has different origins:

- The Rayleigh-Jeans emission of the evolved stellar population is the dominant contribution in early-type galaxies which are poor in gas and dust.

- The dust, irradiated and heated by an underlying continuum, emits a MIR continuum. Large grains are in thermal equilibrium with the radiation field and have a blackbody-like emission. There also exists a population of very small grains (size  $\leq 50 \text{ \AA}$ ) which never reach the thermal equilibrium. These very small grains (hereafter VSG) can get to high temperatures ( $T > 100 \text{ K}$ ) after absorbing one single UV photon. The grains cool down by emission longwards of 10  $\mu\text{m}$  before they absorb new photons. The VSG emission is typical of regions which are actively forming stars, such as HII regions.
- The ionised gas of the interstellar medium emits several strong forbidden lines in the MIR. Lines from Ne, Ar, Si as well as S and Fe are commonly observed in the spectra of AGN (excluding BLLac and OVV) and HII regions. In particular, [ArIII] 8.9  $\mu\text{m}$ , [SIV] 10.4  $\mu\text{m}$  and [NeII] 12.8  $\mu\text{m}$  lie within the wavelength range of the set of filters we used for this study.
- The unidentified infrared bands (UIB) observed at 6.2, 7.7, 8.6, 11.3 and 12.7  $\mu\text{m}$  are characteristic of photodissociation regions (hereafter PDR), where molecules form and their physical conditions depend on the UV photon density. Since the original work of Léger & Puget (1984), these bands are interpreted as the bending and stretching vibration modes of the C=C and C-H links in polycyclic aromatic hydrocarbons (PAH).

In Fig. 1, template spectra over the 7–14  $\mu\text{m}$  range (Laurent et al. 2000) are displayed for the three main types of MIR sources: AGN, HII region and PDR. These templates are useful for comparison with observations: we therefore overplotted on the template spectra the flux densities that would be measured through the TIMMI2 filters.

The AGN spectrum is dominated by continuum emission from the dusty torus, and hard silicate absorption around 9.7  $\mu\text{m}$  can be observed. Usually, PAH emission is absent or very weak since the carriers are destroyed by the strong radiation field.

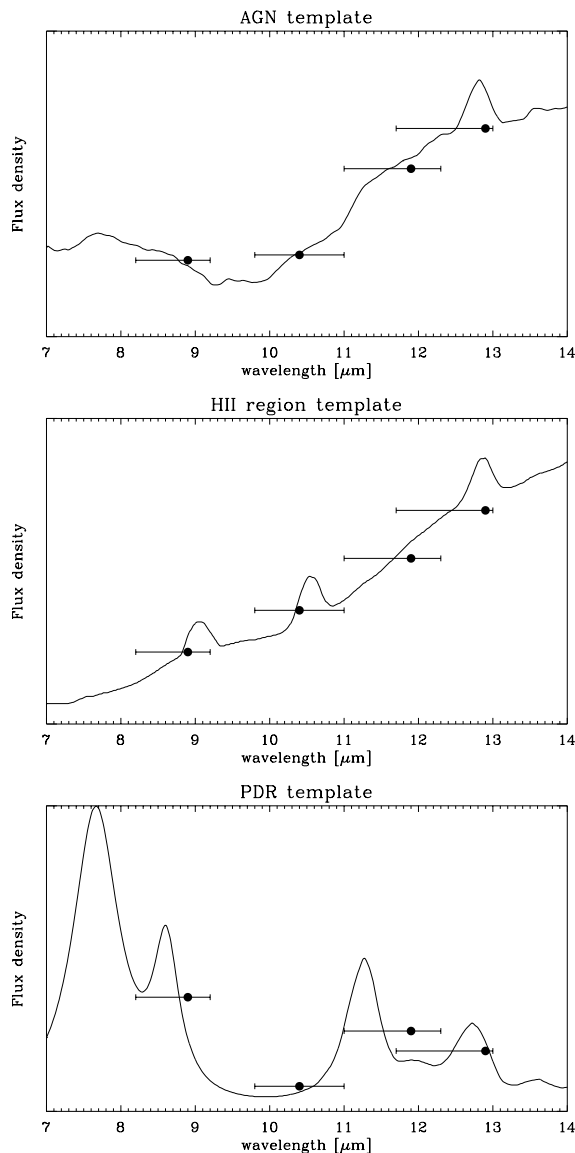


**Fig. 1.** Template spectra for the 7–14  $\mu\text{m}$  emission of the three main types of MIR sources: AGN, HII region and PDR. The spectra are from Laurent et al. (2000). The corresponding flux densities through the 8.9  $\mu\text{m}$ , 10.4  $\mu\text{m}$ , 11.9  $\mu\text{m}$  and 12.9  $\mu\text{m}$  filters are overplotted: the horizontal bar marks the width of the filter, while the abscissa of the dots correspond to the wavelengths of the TIMMI 2 filter names.

The HII region spectrum displays a steeply rising continuum, due to VSG emission. The ionised gas produces the strong [ArIII] 8.9  $\mu\text{m}$ , [SIV] 10.4  $\mu\text{m}$  and [NeII] 12.8  $\mu\text{m}$ , but the PAH carriers are destroyed by the radiation field as in the case of AGN.

The PDR spectrum is dominated by the emission of the PAH. The PDR forms at a distance from the hot stars which is large enough for the UV continuum to be weakened and softened; this allows molecules to be formed in the cool gas.

We shall use the flux ratios computed with these templates to distinguish between the various object types and to help interpret the MIR emission from our sample sources.

### 3. Results

An overview of the observational results is presented in this section. In the first part, we give results for the whole sample, and provide a short general discussion. Then we discuss in more detail the most interesting cases. Table 2 summarises the full set of measurements. For each target, we provide the fluxes and relative positions for all the identified sources. The targets are listed by increasing distance. MIR extended emission (resolved and/or diffuse) is detected in 4 objects: NGC 253, NGC 1808, NGC 1365 and NGC 7469. Contour maps of the emission for these sources are presented in Fig. 2. For each object, the brightest source (which is the AGN except in the case of NGC 253) is labelled M 1, while the circumnuclear sources are labelled M 2, M 3, etc.

#### 3.1. Overview

MIR emission was detected for all the targets in the sample:

- In NGC 253, six distinct sources have been identified in the central region. This provides a gain in spatial resolution with respect to previous observations, which helps clarify the distribution of the MIR emission from this galaxy.
- In Circinus, emission has been detected in all four narrow  $N$ -band filters. This is also the only target that we have detected at 20  $\mu\text{m}$ .
- In NGC 1808 and NGC 1365, a previously unknown population of MIR sources in the inner 10'' region around their AGN is unveiled.
- In NGC 7469, extended diffuse emission is detected around the AGN and shows interesting morphological peculiarities. While the 12.9  $\mu\text{m}$  map shows an emission quite symmetrically distributed around the nucleus, the 10.4  $\mu\text{m}$  map unveils the presence of a bar-like structure along the N-S direction.
- The last four objects, NGC 1992, NGC 5995, IZw1 and IIZw136 are detected, each through two to three filters, as single unresolved sources.

The measured fluxes are generally in good agreement with previous measurements (see dedicated sections hereafter). Most previous measurements had been derived from data obtained with poorer spatial resolution and from photometry performed through much larger apertures than ours, hence encompassing a much larger fraction of the galaxies than the nuclear regions we are probing with TIMMI 2. Therefore, this suggests that most of the MIR emission from these targets is indeed arising in their central  $\sim 10''$  region and can be accounted for by the AGN and the discrete sources revealed in the TIMMI 2 images.

In none of the targets do we find extended MIR emission comparable to that observed in NGC 1068 or 3C 66B along the radio jet (Alloin et al. 2000; Tansley et al. 2000), except a tentative detection in NGC 1365 (see Sect. 3.5). According to the AGN unified scheme, we were expecting to detect collimated MIR emission in the type 2 objects of our sample, which was not the case. An analysis on a larger sample and from images with higher sensitivity is needed to understand the diversity of MIR morphologies of type 2 objects, and is left for future study.

**Table 2.** Photometry of resolved MIR sources for each galaxy in our sample in each N-band filter. The symbol “–” indicates that the source was not observed through the corresponding filter. Source labelling is according to the scheme described in Sect. 3.

| Target                | Individual source name | Flux [mJy] <sup>a</sup><br>8.9 $\mu$ m | Flux [mJy] <sup>a</sup><br>10.4 $\mu$ m | Flux [mJy] <sup>a</sup><br>11.9 $\mu$ m | Flux [mJy] <sup>a</sup><br>12.9 $\mu$ m | Relative position <sup>b</sup><br>$\alpha$ ["] $\delta$ ["] |       |
|-----------------------|------------------------|--|---|---|---|---|-------|
| NGC 253               | M 1                    | –                                      | –                                       | 5100 $\pm$ 1000                         | –                                       | 0   | 0     |
|                       | M 2                    | –                                      | –                                       | 400 $\pm$ 100                           | –                                       | 0.87  | 1.04  |
|                       | M 3                    | –                                      | –                                       | 350 $\pm$ 100                           | –                                       | 1.17  | 1.5   |
|                       | M 4                    | –                                      | –                                       | 500 $\pm$ 100                           | –                                       | 1.99  | 1.29  |
|                       | M 5                    | –                                      | –                                       | 250 $\pm$ 50                            | –                                       | 2.73  | 2.81  |
|                       | M 6                    | –                                      | –                                       | 250 $\pm$ 50                            | –                                       | 4.15  | 3.68  |
|                       | $\sigma$ bg            | –                                      | –                                       | 60                                      | –                                       |   |       |
| Circinus <sup>c</sup> | M 1                    | 7950 $\pm$ 1600                        | 6650 $\pm$ 1350                         | 16 650 $\pm$ 3300                       | 23 400 $\pm$ 4700                       |   |       |
|                       | $\sigma$ bg            | 50                                     | 25                                      | 20                                      | 25                                      |   |       |
| NGC 1808              | M 1                    | –                                      | 255 $\pm$ 50                            | 620 $\pm$ 120                           | 970 $\pm$ 190                           | 0   | 0     |
|                       | M 2                    | –                                      | $\leq$ 10                               | 40 $\pm$ 5                              | 45 $\pm$ 5                              | –1.99   | –3.76 |
|                       | M 3                    | –                                      | 10 $\pm$ 2                              | 50 $\pm$ 10                             | 80 $\pm$ 10                             | –4.55   | 1.39  |
|                       | M 4                    | –                                      | $\leq$ 10                               | 70 $\pm$ 10                             | 170 $\pm$ 30                            | 2.77  | 0.54  |
|                       | M 5                    | –                                      | 23 $\pm$ 5                              | $\leq$ 50                               | 90 $\pm$ 10                             | 2.87  | –1.59 |
|                       | M 6                    | –                                      | $\leq$ 10                               | 75 $\pm$ 10                             | 145 $\pm$ 20                            | 5.82  | –5.25 |
|                       | M 7                    | –                                      | 40 $\pm$ 5                              | 125 $\pm$ 20                            | 90 $\pm$ 20                             | 5.44  | –7.34 |
|                       | M 8                    | –                                      | 15 $\pm$ 5                              | 105 $\pm$ 20                            | 195 $\pm$ 30                            | 2.71  | –5.51 |
|                       | M 9                    | –                                      | 30 $\pm$ 5                              | $\leq$ 40                               | 60 $\pm$ 10                             | 0.70  | –3.38 |
|                       | $\sigma$ bg            | –                                      | 10                                      | 20                                      | 25                                      |   |       |
| NGC 1365              | M 1                    | 410 $\pm$ 80                           | 440 $\pm$ 80                            | 510 $\pm$ 100                           | 1100 $\pm$ 220 <sup>d</sup>             | 0   | 0     |
|                       | M 2                    | $\leq$ 40                              | 20 $\pm$ 4                              | $\leq$ 20                               | $\leq$ 40                               | –4.66   | –5.12 |
|                       | M 3                    | $\leq$ 40                              | 30 $\pm$ 6                              | 30 $\pm$ 6                              | $\leq$ 25                               | –5.40   | –2.56 |
|                       | M 4                    | $\leq$ 40                              | $\leq$ 5                                | 40 $\pm$ 8                              | 160 $\pm$ 30 <sup>a</sup>               | 0.41  | 7.12  |
|                       | M 5                    | $\leq$ 40                              | 60 $\pm$ 10                             | 120 $\pm$ 20                            | 320 $\pm$ 60 <sup>a</sup>               | 2.79  | 9.99  |
|                       | M 6                    | 105 $\pm$ 20                           | 50 $\pm$ 10                             | 140 $\pm$ 20                            | 505 $\pm$ 100 <sup>a</sup>              | 4.75  | 6.95  |
|                       | $\sigma$ bg            | 35                                     | 10                                      | 10                                      | 20                                      |   |       |
| NGC 2992              | M 1                    | –                                      | 230 $\pm$ 45                            | –                                       | 565 $\pm$ 110                           |   |       |
|                       | $\sigma$ bg            | –                                      | 18                                      | –                                       | 33                                      |   |       |
| NGC 7469              | $\odot = 2''$          | –                                      | 310 $\pm$ 60                            | 565 $\pm$ 110                           | –                                       |   |       |
|                       | $\odot = 5.6''$        | –                                      | 450 $\pm$ 90                            | 980 $\pm$ 200                           | –                                       |   |       |
|                       | $\sigma$ bg            | –                                      | 10                                      | 10                                      | –                                       |   |       |
| NGC 5995              | M 1                    | 310 $\pm$ 60                           | –                                       | 300 $\pm$ 60                            | –                                       |   |       |
|                       | $\sigma$ bg            | 100.                                   | –                                       | 25.                                     | –                                       |   |       |
| IZw1                  | M 1                    | –                                      | 375 $\pm$ 75                            | 425 $\pm$ 85                            | 325 $\pm$ 65                            |   |       |
|                       | $\sigma$ bg            | –                                      | 10                                      | 18                                      | 16                                      |   |       |
| IIZw136               | M 1                    | –                                      | 130 $\pm$ 25                            | 130 $\pm$ 25                            | –                                       |   |       |
|                       | $\sigma$ bg            | –                                      | 13                                      | 13                                      | –                                       |   |       |

None of the individual sources from this table are resolved on the TIMMI 2 images, except tentatively NGC 1365/M 1 (see Sect. 3.5). The linear upper limits for the source sizes are, given the galaxy distances of Table 1:

NGC 253: 12 pc; Circinus: 7 pc; NGC 1808: 40 pc; NGC 1365: 70 pc; NGC 2992: 120 pc; NGC 7469: 250 pc for the central peak; NGC 5995: 400 pc; IZw1 and IIZw136: 1 kpc.

<sup>a</sup> Unit for the fluxes is mJy and the unit for  $\sigma$  bg is mJy arcsec<sup>–2</sup>. For most sources, the quoted error is the 20% calibration error (see Sect. 2.3) which dominates over the measurement uncertainty on the images. In cases where the measurement uncertainty was not negligible compared to the 20% error, it was included.

<sup>b</sup> The positions are offsets on our MIR images, relative to source M 1, the coordinates of which are set to (0'', 0''). No significant astrometry is possible with this TIMMI 2 data set because of the small field of view. For NGC 253, a discussion on the coordinates of M 1 (corresponding to the 0'', 0'' position in this table) is provided in Sect. 3.2. For NGC 1808, M 1 can be identified to its counterpart on the cm image (see Sect 3.4), The B1950 coordinates of the M 1 cm counterpart derived by Saikia et al. (1990) are RA: 05<sup>h</sup>05<sup>m</sup>58.56<sup>s</sup>, Dec: –37°34'36.3'', with no information concerning the uncertainty. For NGC 1365, the B1950 coordinates of M 1 radio counterpart are RA: 03<sup>h</sup>31<sup>m</sup>41.80<sup>s</sup>, Dec: –36°18'26.8'' (Sandqvist et al. 1995, no information on the uncertainty). This cm image is shown in Sect. 3.5.

<sup>c</sup> Circinus was also detected at 20  $\mu$ m, with a flux of 30  $\pm$  6 Jy and  $\sigma$  bg of 1.2 Jy arcsec<sup>–2</sup>.

<sup>d</sup> The photometric calibration used for NGC 1365 at 12.9  $\mu$ m may be greater than the actual one by up to a factor two because of local sky transparency variations (see Sect. 2.3). This would result in flux values that are up to twice smaller.

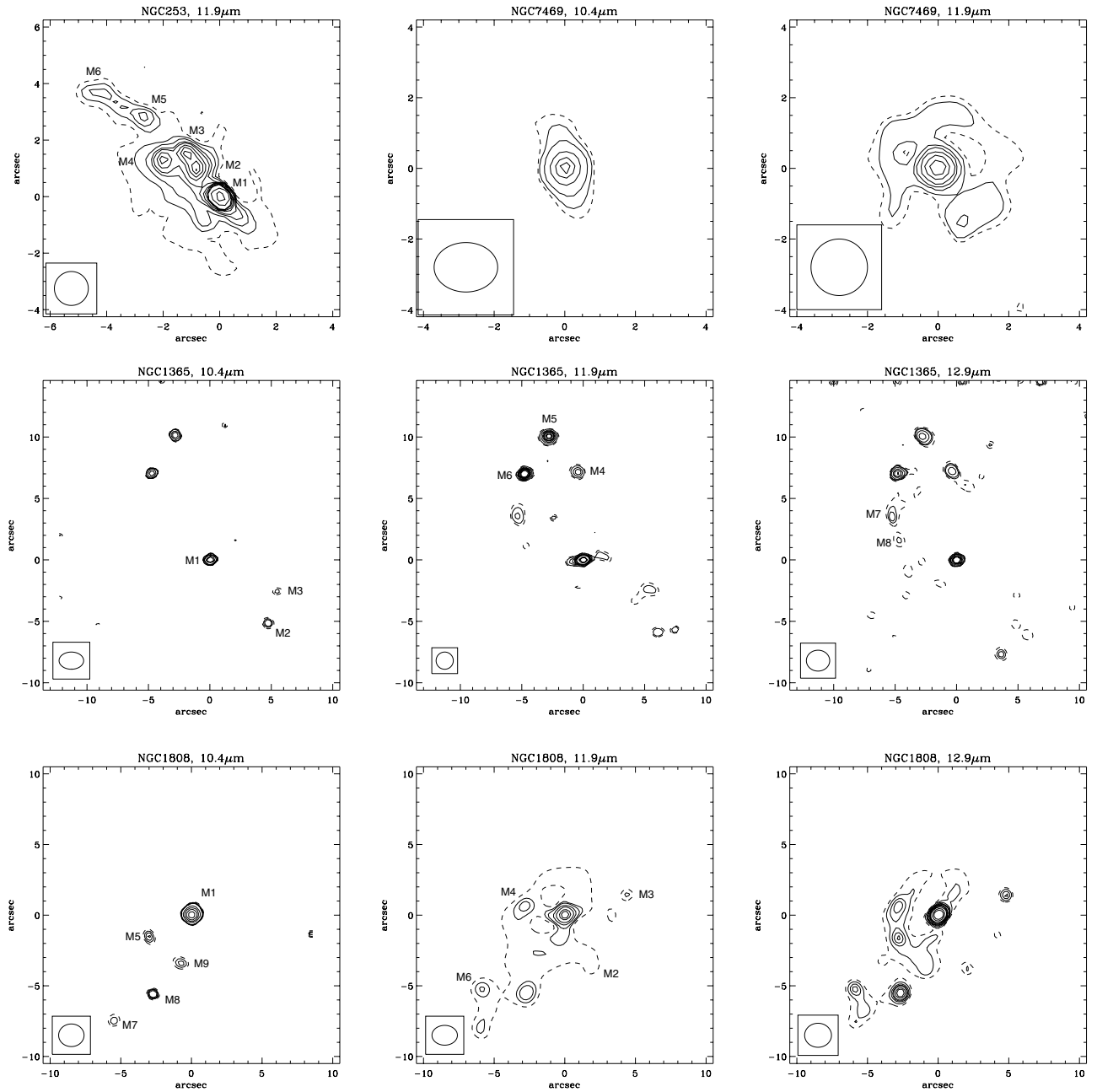


**Fig. 2.** Deconvolved maps for the objects with resolved emission. North is up and East left. Dotted contours correspond to  $1\sigma$  of the background. Source labelling is according to the scheme described in Sect. 3. Galaxy and filter identifications are given as a title for each panel. The lower left square on each panel displays the corresponding PSF shape ( $FWHM$  in the E-W and N-S directions).

In the following, we present, in some detail, the results obtained for NGC 253, Circinus, NGC 1808, NGC 1365, NGC 7469.

### 3.2. NGC 253: MIR detection of the radio nucleus?

NGC 253 hosts a vigorous starburst in its inner 100 pc central region and is the archetypal starburst galaxy. Turner & Ho (1985) discovered a set of highly aligned compact radio sources along the  $\sim$ NE-SW direction. Ulvestad & Antonucci (1997), performed high resolution and sensitive VLA observations and identified 64 sources. These sources probably

belong to a nuclear ring seen at high inclination, and thus appear in a string-like distribution. The most powerful of these radio sources (TH-2) is considered to be the true nucleus of NGC 253, and is thought to be an AGN (Forbes et al. 2000). Imaging of NGC 253 has been carried out in the NIR (Forbes et al. 1991, 1993; Sams et al. 1994; Kalas & Wynn-Williams 1994) and MIR (Pina et al. 1992; Keto et al. 1993; Böker et al. 1998; Keto et al. 1999). These observations show that the NIR/MIR emission consists of a bright, barely elongated source plus a secondary, fainter source to the NE of the brightest one. The brightest NIR/MIR source is believed to be a young massive star cluster (Keto et al. 1999). Both sources are inside an

elongated envelope, with a PA similar to that of the radio string. However, a general lack of correlation between the IR and the radio sources is observed.

The TIMMI 2 image of NGC 253 (through the  $11.9\ \mu\text{m}$  filter) is the highest resolution MIR image of this galaxy available to date. The MIR morphology revealed in this image is fully consistent with the previous MIR observations at lower angular resolution, but the distribution of the emission is resolved into six discrete sources. The flux measurement at  $11.7\ \mu\text{m}$  made by Pina et al. (1992) of M 1 is best suited for comparison with our  $11.9\ \mu\text{m}$  flux. Their flux of 4.8 Jy is in good agreement with ours ( $5.1 \pm 0.1$  Jy). Comparison cannot be made with fluxes in the other filters because of the presence of strong emission lines and PAH bands (Kalas & Wynn-Williams 1994; Keto et al. 1999).

Again, at the resolution achieved with TIMMI 2, the source distributions in the radio and in the MIR are not obviously coincident, even though the global position angle of both distributions is the same.

We propose two registrations of our MIR map with respect to the 2 cm map by Ulvestad & Antonucci (1997):

(a) We use the absolute registration of M 1 performed by Keto et al. (1993). It is consistent with other measurements from Pina et al. (1992) and Kalas & Wynn-Williams (1994), and has the smallest uncertainty (about  $0.4''$ ): the measurement of the position of M 1 gives  $\alpha(1950) = 00^{\text{h}}45^{\text{m}}5.630^{\text{s}} \pm 0.026^{\text{s}}$  and  $\delta(1950) = -25^{\circ}33'40.57'' \pm 0.44''$ . The resulting superposition of the MIR map and the radio sources is displayed in Fig. 3b. We do not believe this blind registration to be the correct one, since the MIR string and the radio string are shifted with respect to the other. However, under this registration, M 4 is coincident with the radio nucleus.

(b) We try to align the MIR and radio peaks. To do so, we simply minimise the sum, over all the MIR sources, of the distances to the closest radio source. Figure 3c shows the resulting map. This registration suggests, this time, that source M 3 is the counterpart of the radio nucleus. The superposition is globally much more convincing than the blind one. In this case, the B1950 coordinates of M 1 can be derived:  $\alpha = 00^{\text{h}}45^{\text{m}}5.703^{\text{s}}$  and  $\delta = -25^{\circ}33'40.57''$ . These coordinates are not consistent, within the quoted error boxes, with the absolute coordinates of M 1 derived by Keto et al. (1993), but are consistent with those, with larger error bar, by Pina et al. (1992) and Kalas & Wynn-Williams (1994).

Despite the inconsistency with Keto's measurement, we favour the second registration, for which the string of radio sources is well aligned with the MIR emission. In none of these registrations does source M 1 have a radio counterpart. The lack of radio emission from M 1, already discussed by Forbes et al. (2000), is confirmed by our study and remains mysterious. And finally, our preferred registration places the radio nucleus in coincidence with the MIR source M 3.

### 3.3. Circinus: still point like at $0.6''$ resolution

Circinus is the closest type 2 AGN, at a distance of only 4 Mpc. The nuclear region harbours a heavily obscured

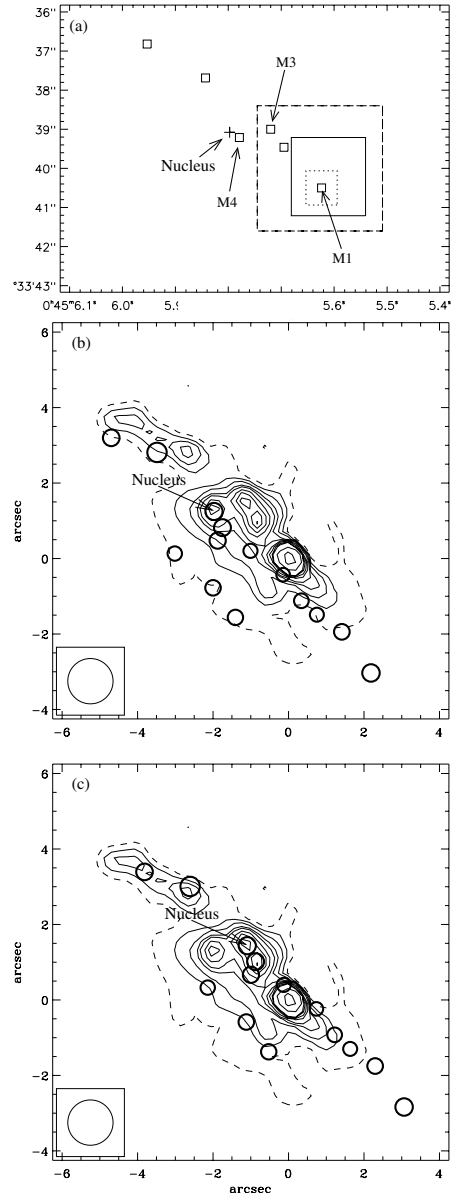


**Fig. 3.** NGC 253, two tentative registrations of the MIR map (contours) with respect to the radio map (brightest sources shown by circles). The radio map was obtained by Ulvestad & Antonucci (1997) at 2 cm. **a)** Absolute astrometry of the NIR/MIR images. The three boxes show the absolute (B1950) positions and positional errors for the bright NIR/MIR source M 1: the dashed, solid and dotted line boxes show the respective registrations of Pina et al. (1992), Kalas & Wynn-Williams (1994) and Keto et al. (1993). The small squares ( $0.2''$  side) record the positions of the TIMMI2 sources with the brightest source M 1 assigned at the most probable absolute position of peak1 as derived by Keto et al. (1993). The cross marks the absolute position of the radio nucleus. **b)** Blind registration: M 1 is positioned at the coordinates derived by Keto et al. (1993). **c)** Best registration: tentative alignment of the MIR and radio peaks. As in Fig. 2, the lower left square on each panel displays the PSF.

AGN ( $N_{\text{H}} \geq 10^{24}\ \text{cm}^{-2}$  based on X-ray data by Matt et al. 1999). It also exhibits a prominent ionisation cone extending to the NW, and a starburst ring at a radius of about  $10''$  ( $\sim 100$  pc) from the nucleus (Davies et al. 1998). Circinus has been

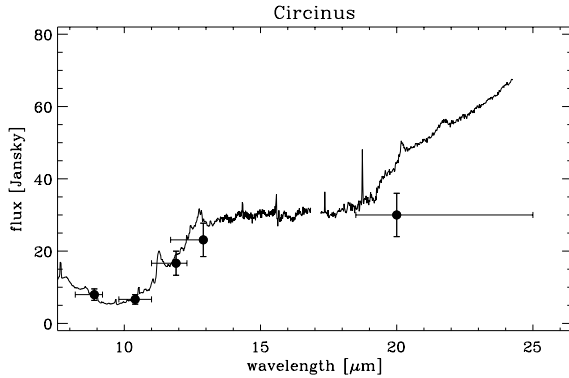


**Fig. 4.** Photometric measurements for the Circinus galaxy. The filled circles show our measurements. The ISO spectrum from Sturm et al. (2000) is overplotted for comparison.

previously imaged at high resolution with TIMMI (Siebenmorgen et al. 1997) and MANIAC (Krabbe et al. 2001), both showing marginal extension of the central source. The latter study also revealed the presence of a low surface brightness diffuse halo of radius  $\sim 10''$ .

Aperture photometry was performed to obtain the  $N$ -band fluxes for Circinus within an aperture of  $2''$  radius. This radius was optimised using a curve of growth analysis. The background was measured in an annulus around this aperture (with inner and outer radii  $2''$  and  $4''$ , respectively). The TIMMI 2 data points are plotted in Fig. 4. The  $14'' \times 20''$  aperture ISO-SWS spectrum by Sturm et al. (2000) is shown. The  $N$ -band TIMMI 2 measurements are in good agreement with the ISO spectrum, showing that the entire MIR emission comes from the nuclear source. At  $20 \mu\text{m}$ , the discrepancy between the TIMMI 2 data and the ISO spectrum is difficult to interpret in a decisive manner. Observing and calibrating ground based data in this window is a difficult task. Moreover, the  $20 \mu\text{m}$  emission is expected to be more extended than the  $10 \mu\text{m}$  one, since it traces cooler material. Undetected diffuse emission on a scale of the order of  $10''$ , could be responsible for this difference.

On the TIMMI 2 data, the comparison between the AGN and the corresponding standard star profiles does not reveal any sign of resolved emission in Circinus on a scale  $0.3\text{--}0.4''$  ( $5.5\text{--}7.5 \text{ pc}$ ). The TIMMI 2 image reaches a  $1\sigma$  background level of  $25 \text{ mJy arcsec}^{-2}$ , which is insufficient to detect the broad  $N$ -band halo emission claimed by Krabbe et al. in 2001 ( $17 \text{ mJy arcsec}^{-2}$ ).

### 3.4. NGC 1808: MIR detection of radio sources

NGC 1808 is a morphologically peculiar spiral galaxy ( $5 \text{ kpc}$ ) located at a distance of  $10.9 \text{ Mpc}$  (Koribalski et al. 1996). The nature of its nuclear source is not yet clearly established. Véron-Cetty & Véron (1985) concluded to the presence of an AGN, while Forbes et al. (1992) proposed instead that the nucleus consists of a SNR embedded within a metal-rich HII region. NGC 1808 has been detected in hard X-rays (Awaki & Koyama 1993; Junkes et al. 1995), suggesting that an embedded AGN is indeed present in the nuclear region. However, Krabbe et al. (2001) show that, in a MIR vs. X-ray flux

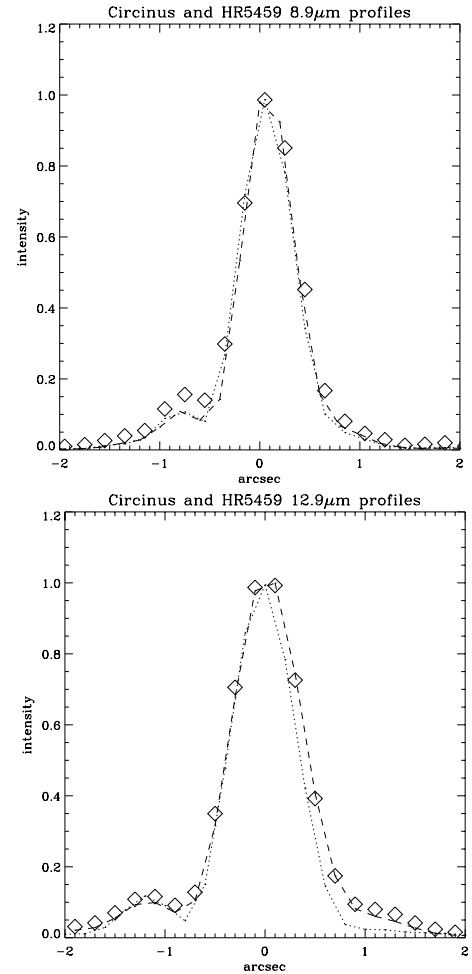


**Fig. 5.** Circinus: profiles along the E-W direction at  $8.9 \mu\text{m}$  (top) and  $12.9 \mu\text{m}$  (bottom). The squares feature the profile of Circinus and its sampling, while the dashed and dotted lines show the profiles of the standard star HR5459, acquired before and after Circinus, respectively.

diagram, the location of NGC 1808 argues against the presence of an AGN.

The central region (inner  $\sim 750 \text{ pc}$ ) of NGC 1808 is undergoing an episode of enhanced star formation. There were early reports on the presence of “hot spots” in its complex nuclear region by Morgan (1958) and Sérsic & Pastoriza (1965). Strong PAH emission was observed by Siebenmorgen et al. (2001) from the star-forming region. Radio continuum observations (Saikia et al. 1990; Collison et al. 1994) revealed a population of compact radio sources, most of which do not coincide with the optical hot spots. According to Saikia et al. (1990), they are more likely related to young SNRs than due to the thermal emission from giant HII regions. A high resolution  $K$ -band image was published by Tacconi-Garman et al. (1996), showing the presence of many distinct and compact ( $\leq 0.7''$ ) sources spread all over the circumnuclear region. These authors argue that such sources are likely to be clusters containing hundreds of massive red super-giants. Not all of the radio emitting sources have counterparts in the map by

**Table 3.** Compiled NIR-MIR photometry for the galaxies in our sample. The MIR data presented here are the integrated fluxes over the aperture given in the table.

| Name                 | Wavelength<br>[ $\mu\text{m}$ ] | Aperture<br>[arcsec] | Projected<br>size [pc] | Flux<br>[mJy]      | Reference                    | $\log(\nu L_\nu)$<br>[ $\text{erg.s}^{-1}$ ] |
|----------------------|---------------------------------|----------------------|------------------------|--------------------|------------------------------|--|
| Circinus<br>2.5 Mpc  | 1.265                           | 0.19                 | 3.6                    | $1.6 \pm 0.2$      | Prieto et al. (2004)         | 39.9   |
|                      | 1.66                            | 0.19                 | 3.6                    | $4.77 \pm 0.5$     | "                            | 40.2   |
|                      | 2.18                            | 0.19                 | 3.6                    | $19 \pm 1.9$       | "                            | 40.7   |
|                      | 3.80                            | 0.19                 | 3.6                    | $380 \pm 38$       | "                            | 41.8   |
|                      | 4.78                            | 0.19                 | 3.6                    | $1900 \pm 190$     | "                            | 42.4   |
|                      | 8.9                             | 2                    | 38                     | $7950 \pm 1590$    | This work                    | 42.7   |
|                      | 10.4                            | 2                    | 38                     | $6650 \pm 1330$    | "                            | 42.6   |
|                      | 11.9                            | 2                    | 38                     | $16\,650 \pm 3330$ | "                            | 42.9   |
|                      | 12.9                            | 2                    | 38                     | $23\,400 \pm 4680$ | "                            | 43.0   |
|                      | 20                              | 2                    | 38                     | $30\,000 \pm 6000$ | "                            | 42.9   |
| NGC 1808<br>10.9 Mpc | 2.2                             | 2                    | 106                    | $43.5 \pm 4.4$     | Galliano, in preparation     | 41.9   |
|                      | 3.5                             | 2                    | 106                    | $36.9 \pm 7.4$     | "                            | 41.7   |
|                      | 4.8                             | 2                    | 106                    | $19.1 \pm 3.8$     | "                            | 41.2   |
|                      | 10.4                            | 2                    | 106                    | $255 \pm 51$       | This work                    | 42.0   |
|                      | 11.9                            | 2                    | 106                    | $620 \pm 124$      | "                            | 42.3   |
|                      | 12.9                            | 2                    | 106                    | $970 \pm 194$      | "                            | 42.5   |
| NGC 1365<br>18.6 Mpc | 2.2                             | 2                    | 106                    | $78 \pm 7.8$       | Galliano, in preparation     | 42.6   |
|                      | 3.5                             | 2                    | 106                    | $205 \pm 41$       | "                            | 42.9   |
|                      | 4.8                             | 2                    | 106                    | $177 \pm 35$       | "                            | 42.7   |
|                      | 8.9                             | 2                    | 180                    | $410 \pm 82$       | This work                    | 42.8   |
|                      | 10.4                            | 2                    | 180                    | $440 \pm 88$       | "                            | 42.7   |
|                      | 11.9                            | 2                    | 180                    | $510 \pm 102$      | "                            | 42.7   |
|                      | 12.9                            | 2                    | 180                    | $110 \pm 220$      | "                            | 43.0   |
| NGC 2992<br>301. Mpc | 2.18                            | 3                    | 450                    | $^a 2.8 \pm 0.2$   | Alonso-Herrero et al. (2001) | 41.6   |
|                      | 3.8                             | 3                    | 450                    | $^a 22.7 \pm 2.0$  | "                            | 42.3   |
|                      | 4.8                             | 3                    | 450                    | $^a 35.7 \pm 10.7$ | "                            | 42.4   |
|                      | 10.4                            | 2                    | 300                    | $230 \pm 46$       | This work                    | 42.9   |
|                      | 12.9                            | 2                    | 300                    | $565 \pm 110$      | "                            | 43.2   |
| NGC 7469<br>66 Mpc   | 1.1                             | 3                    | 960                    | $^a 16.2 \pm 2.4$  | Alonso-Herrero et al. (2001) | 43.4   |
|                      | 1.6                             | 3                    | 960                    | $^a 39 \pm 5.9$    | "                            | 43.6   |
|                      | 2.22                            | 3                    | 960                    | $^a 67.8 \pm 17.0$ | "                            | 43.7   |
|                      | 3.80                            | 3                    | 960                    | $^a 159 \pm 4.8$   | Ward et al. (1987)           | 43.8   |
|                      | 4.78                            | 3                    | 960                    | $^a 259 \pm 31$    | "                            | 43.9   |
|                      | 10.4                            | 2                    | 640                    | $310 \pm 62$       | This work                    | 43.7   |
|                      | 11.9                            | 2                    | 640                    | $565 \pm 113$      | "                            | 43.9   |
| NGC 5995<br>100 Mpc  | 2.2                             | 10                   | 3200                   | $38 \pm 0.8$       | Hunt et al. (1999)           | 43.8   |
|                      | 8.9                             | 2                    | 980                    | $310 \pm 62$       | This work                    | 44.1   |
|                      | 11.9                            | 2                    | 980                    | $300 \pm 60$       | "                            | 44.0   |
| IZw1<br>245 Mpc      | 3.5                             | 8.5                  | 10 000                 | $110 \pm 11$       | Rieke (1978)                 | 44.8   |
|                      | 10.4                            | 2                    | 2370                   | $375 \pm 75$       | This work                    | 44.9   |
|                      | 11.9                            | 2                    | 2370                   | $425 \pm 85$       | "                            | 44.9   |
|                      | 12.9                            | 2                    | 2370                   | $325 \pm 65$       | "                            | 44.7   |
| II Zw 136<br>252 Mpc | 10.4                            | 2                    | 2440                   | $130 \pm 26$       | This work                    | 44.5   |
|                      | 11.9                            | 2                    | 2440                   | $130 \pm 26$       | "                            | 44.4   |

<sup>a</sup> Non-stellar contribution, as computed by Alonso-Herrero et al. (2001).

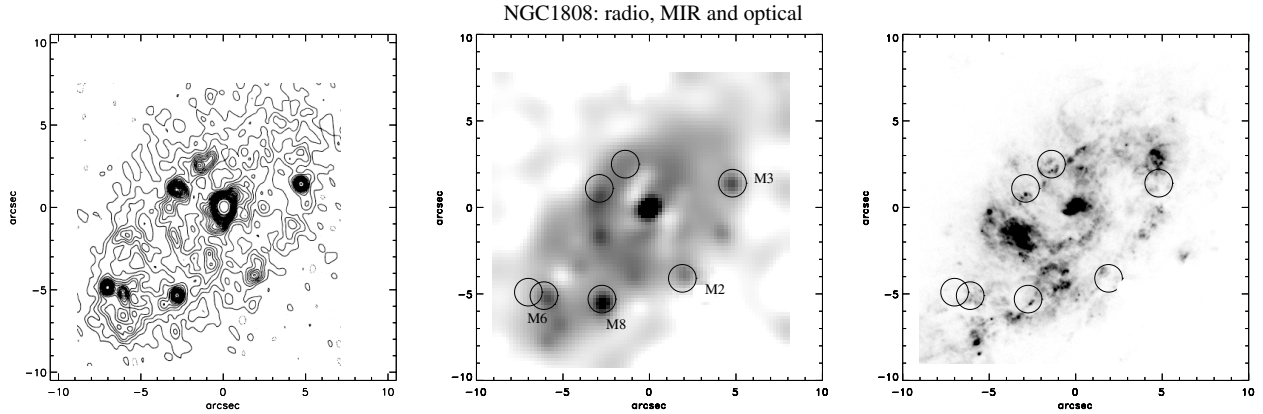


**Fig. 6.** NGC 1808: *from left to right*, radio, MIR and optical images. The map at 3.6 cm is from Collison et al. (1994); our TIMMI 2 map at  $12.9\ \mu\text{m}$  is displayed with a non-linear flux scale in order to highlight faint structures; the HST image ( $F658N$ ) is from the HST archive. On the MIR and optical maps, the locations of the main radio sources are marked by circles of radius  $0.8''$ .

Tacconi-Garman et al. (1996). Particularly, the three brightest circumnuclear radio sources have no NIR counterpart.

Krabbe et al. (2001) found a nuclear flux of  $0.33\ \text{Jy}$  through an  $N$ -band ( $8\text{--}13\ \mu\text{m}$ ) filter. This value is in reasonable agreement with ours (see Table 3) although a precise comparison is not possible because of the different filters used. The  $12.9\ \mu\text{m}$  map of the central region of NGC 1808 is reproduced in Fig. 6 together with the 3.6 cm image obtained by Collison et al. (1994) and an HST archive image in the optical ( $F658N$ ). The radio and MIR maps are strikingly similar. The most intense radio sources are featured by circles of arbitrary  $0.8''$  radius on the MIR and optical maps. Several of the intense radio sources have a counterpart on the MIR image. Particularly, this comparison shows that M 2, M 3, M 6 and M 8 are also radio sources. On the HST image, counterparts for the MIR/radio sources are not clearly detected, but may be identified to faint sources that can be seen inside the circles in Fig. 6. M 8 is the source that has most likely an optical counterpart. A comparison between a higher resolution MIR map and the HST image is needed in order to investigate which optical sources are the counterparts of the MIR/radio sources. Still, it is clear that the regions of most intense optical emission (the hot spots) do not coincide with either radio or MIR sources. The nature of these MIR/radio sources will be discussed in detail in Sect. 5.

### 3.5. NGC 1365: MIR detection of radio sources

A global picture of NGC 1365 can be found in the review by Lindblad (1999). This spiral galaxy with a prominent bar has been classified as SBb(s)I (Sandage & Tammann 1981). An estimate of its distance is discussed in Lindblad (1999) and is currently  $18.6 \pm 0.6\ \text{Mpc}$ . At this distance,  $1''$  corresponds to  $90\ \text{pc}$ . The nuclear region harbours an AGN as shown by the presence of both broad and narrow Balmer emission lines, as well as narrow and strong forbidden emission lines of high excitation (Véron et al. 1980; Alloin et al. 1981). It is classified as a type 1.5 AGN, but varies from type 1 to type 2 according to the level of its hard radiation emission.

It has long been known to show interesting structures in its nuclear region (Sérsic & Pastoriza 1965). In the optical, this region shows several bright hot spots within 1 kpc around the AGN. The HST images resolve the circumnuclear region into a large number of bright, compact star clusters of only a few parsec radii (Kristen et al. 1997; Lindblad 1999). In the radio domain, continuum observations have been performed at 20, 6 and 2 cm with the VLA (Sandqvist et al. 1982; Saikia et al. 1994; Sandqvist et al. 1995) and at 6 and 3 cm by Forbes & Norris (1998) with the Australian Compact Array (ATCA). These maps show that the nucleus is surrounded by several non-thermal radio sources, while the AGN itself is not a particularly strong radio source. The radio sources do not coincide with the bright optical knots. A set of NIR images of the nuclear region of NGC 1365 at very good spatial resolution ( $\sim 0.3''$ ) were taken during the commissioning of ISAAC at the VLT by Moorwood et al. (1998): very red ( $K - L \approx 4$ ) counterparts to the brightest radio sources were detected, suggesting the presence of deeply embedded sources.

Very few MIR observations of NGC 1365 have been performed to date. Frogel et al. (1982) made a series of MIR measurements that are only consistent within a factor of two with our recent measurements. Such a difference can have various origins (differences in filter shape, aperture, and even, over this 20 years period, genuine variations of the MIR emission of the AGN). The map at  $11.9\ \mu\text{m}$  reveals a  $4''$  extension centred on the nucleus (M 1) along the E-W direction (Fig. 2). This extension does not clearly appear on the other maps. At  $10.4$ ,  $11.9$  and  $12.9\ \mu\text{m}$ , the nuclear source (M 1) itself presents a slight ( $2''$ ) extension in the E-W direction which is absent in the other MIR sources in the field. Therefore, we believe that this extension is real. Indeed, to the East of the nucleus, a radio “jet-like” structure between the nucleus and the radio source F has been observed by Sandqvist et al. (1995). Thus the MIR and radio emissions of this extended feature might be related. Figure 7 compares, at the same scale, the maps in the visible, in the radio and in the MIR. Both sources M 2 and M 3, are clearly detected at  $10.4\ \mu\text{m}$ , while at  $11.9\ \mu\text{m}$  only M 3 shows up and neither of them is detected at  $12.9\ \mu\text{m}$ . This indicates that M 2 and M 3 are not strong dust emitters, with a

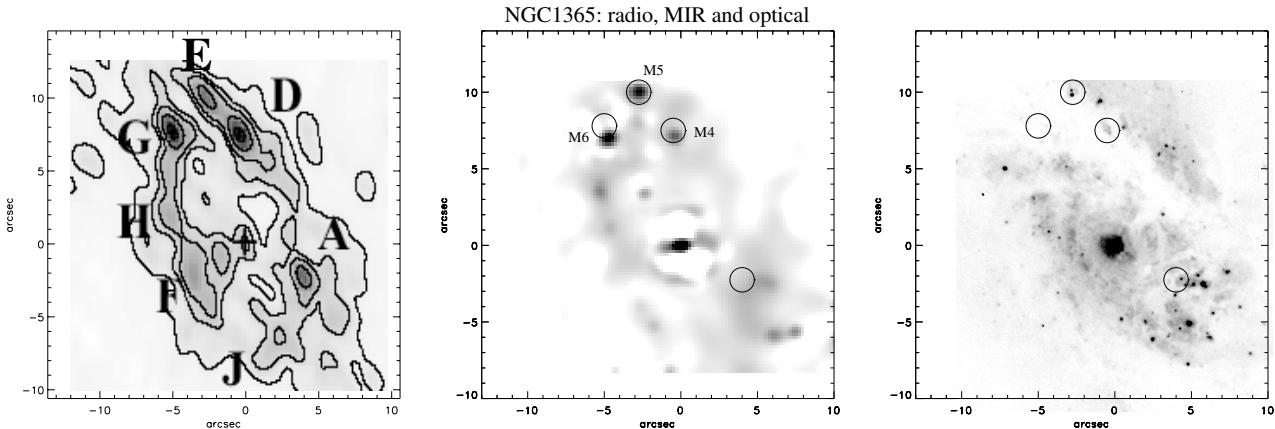


**Fig. 7.** NGC 1365: *from left to right*: radio, MIR and optical images. The map at 3 cm is from Forbes & Norris (1998); our TIMMI 2 map at  $11.9 \mu\text{m}$  is displayed with a non-linear flux scale in order to highlight faint structures and the HST image (*F814W*) is from the archive. On the MIR and optical maps, the locations of the main 3 cm sources are marked by circles of radius  $0.8''$ .

rather flat or decreasing MIR spectrum and no PAH emission. The comparison between the radio and the MIR maps shows that, as in the case of NGC 1808, the bright radio sources have a counterpart in the MIR, while they do not coincide with any strong optical feature. The coincidence between M 6 and the radio source G is not perfect, if using the map by Forbes & Norris (1998). Comparison with the 2 cm map by Saikia et al. (1994) gives a much better coincidence. This kind of discrepancies may come from the uncertainty in the reconstruction of radio maps when the emission is from an extended component together with point-like sources. We conclude that sources M 4, M 5 and M 6 are the respective counterparts of radio sources D, E and G. The optical HST image clearly shows the presence of a dust lane to the north of the AGN. At the location of M 6, no optical source is detected, which is understandable as M 6 lies in the middle of the dust lane. Two optical sources are present at the location of M 5 and might be its counterpart. An extended cone-shaped optical source appears at the location of M 4, and may be related to it. The nature of the MIR/radio sources in NGC 1365 is discussed, together with those observed in NGC 1808, in Sect. 5.

### 3.6. NGC 7469

NGC 7469 shows a type 1 AGN hosted in an SBa galaxy. A significant fraction of the nuclear luminosity originates in a circumnuclear ring of star formation (1 kpc diameter), which is seen face-on and thus appears more or less symmetrical around the AGN. The circumnuclear ring has been detected in the optical (speckle imaging by Mauder et al. 1994), NIR (Marco & Alloin 1998) and MIR (Miles et al. 1994), while PAH emission has been observed by Mazzarella et al. (1994) and Miles et al. (1994). Non-thermal radio continuum emission is detected both as an extended component and as several knots located  $1.5''$  to  $2''$  away from the nucleus (Ulvestad et al. 1981; Condon et al. 1982; Wilson et al. 1991), hence belonging to the star formation ring.

The  $10.4 \mu\text{m}$  flux measured from the TIMMI 2 dataset for the central source is in good agreement with the *N*-band

measurement from Gorjian et al. (2004). The morphology seen on the TIMMI 2 map at  $11.9 \mu\text{m}$  is consistent with high resolution NIR images, particularly the  $0.4''$  resolution J and H SHARP maps published by Genzel et al. (1995): the circumnuclear ring shows enhanced brightness to the NE and SW. Surprisingly, the  $10.4 \mu\text{m}$  image has a quite different aspect and reveals only an extension along the  $\sim$ N-S direction. A simple interpretation is that, except along the N-S axis, the extended MIR emission is dominated by PDR emission, with low continuum at  $10.4 \mu\text{m}$  and intense PAH emission in the  $11.9 \mu\text{m}$  filter. An additional N-S micro-bar with large dust content could explain the observed intense N-S emission at  $10.4 \mu\text{m}$ .

### 3.7. Unresolved galaxies

NGC 2992 is an almost edge-on Sa galaxy, interacting with NGC 2993. It is at a distance of 30 Mpc, which gives a scale of  $150 \text{pc}''$ . It harbours a type 2 AGN, located behind a prominent dust lane extending along the major axis of the galaxy. The radio source at the location of the AGN is peculiar in shape (shape of a “Fig. 8”) and extends up to 450 pc (Chapman et al. 2000). The nuclear region of NGC 2992 was observed through the TIMMI 2 10.4 and  $12.9 \mu\text{m}$  filters. We did not detect any conspicuous diffuse/extended emission down to a level of  $35 \text{mJy arcsec}^{-2}$  ( $1\sigma$ ) at  $12.9 \mu\text{m}$ . The AGN appears as a point-like source with  $FWHM = 0.9''$  on the  $10.4 \mu\text{m}$  image. The flux measurements are in agreement with the measurements by Gorjian et al. (2004). The  $12.9/10.4$  flux ratio has a value of 2.44, compatible with both the AGN and PDR templates, and thus PAH bands may be present. A detection of the  $11.3 \mu\text{m}$  PAH band was claimed by Roche et al. (1991), although Mizutani et al. (1994) did not confirm this result as they did not find the PAH signature at  $3.3 \mu\text{m}$ .

NGC 5995 hosts a type 2 AGN and is located at 100 Mpc, leading to a scale of  $490 \text{pc}''$ . It has been observed with TIMMI 2 through the  $8.9$  and  $11.9 \mu\text{m}$  filters. Comparable flux values were found in both filters, suggesting emission from a PDR. The  $11.9 \mu\text{m}$  flux is found to be slightly lower than, but

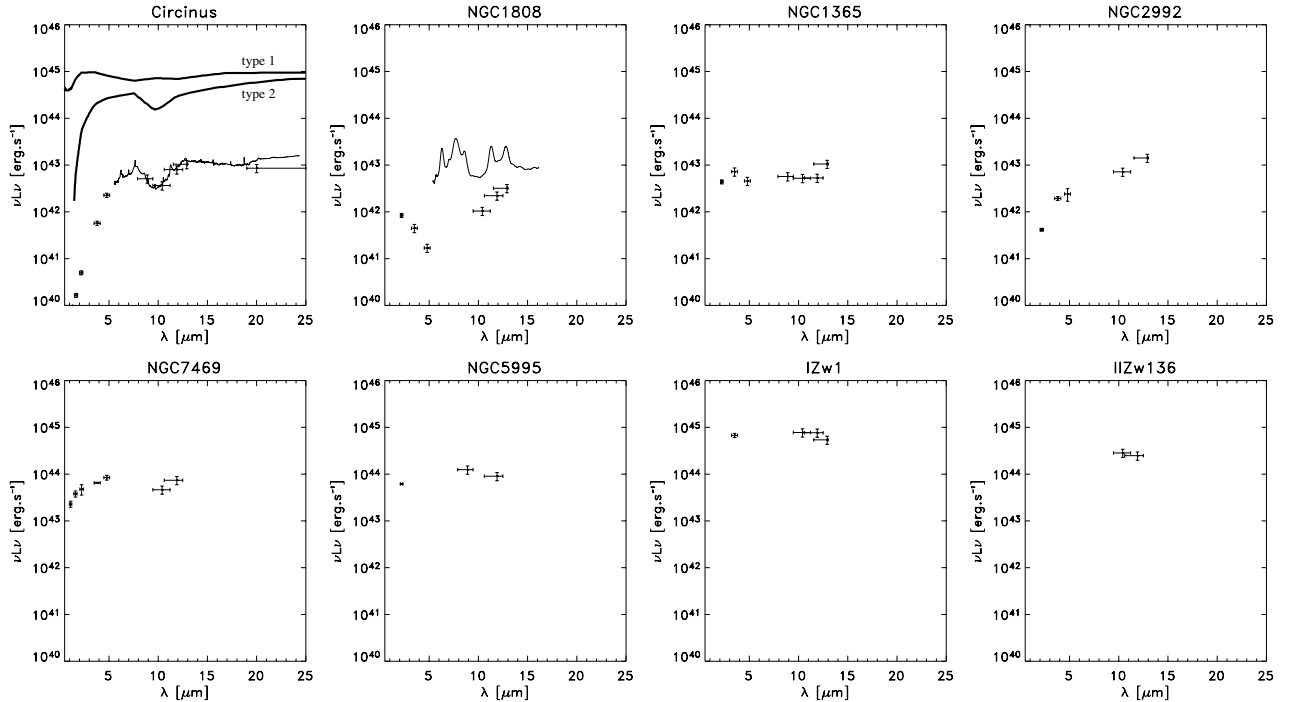


**Fig. 8.** NIR-MIR spectral energy distributions for the AGN in our sample. Intrinsic luminosities have been calculated using the distances reported in Table 1 and they are provided in Table 3. The vertical bar attached to each point represents the photometric uncertainty, while the horizontal bar represents the width of the filter through which the measurement has been performed. Large aperture ISO-SWS spectra (thin continuous line) are overplotted for Circinus and NGC 1808. In the top-left panel, we have overplotted with thick lines modelled typical SED for type 1 and type 2 AGN (Granato et al. 1997, Fig. 1, second model). For the sake of clarity, the flux level of these model SEDs has been set at a large value.

consistent with, the IRAS flux value, implying that most of the MIR emission is from the central source.

IZw1 is the archetypal narrow-line type 1 AGN. It is considered as the closest QSO because of its large intrinsic optical luminosity. At a distance of 245 Mpc, the linear scale is  $1200 \text{ pc}''$ . Schinnerer et al. (1998) find a strong starburst in a circumnuclear ring of  $\sim 1.5''$  in diameter (1.8 kpc). IZw1 was observed with TIMMI2 at 10.4, 11.9 and  $12.9 \mu\text{m}$ . The fluxes are found to be in good agreement with the IRAS ones, indicating that the bulk of the MIR emission comes from the unresolved nucleus. Interestingly, the  $12.9 \mu\text{m}$  flux is significantly lower than the  $11.9 \mu\text{m}$  flux (as in the case of PDR emission), and is at the same level as the  $10.4 \mu\text{m}$ , which is not expected for a PDR emission. This suggests the presence of the silicate feature in emission. Spectroscopy in the MIR should allow to confirm this prediction.

IIZw136 is a type 1 AGN, 252 Mpc away (scale of  $1200 \text{ pc}''$ ). It has been observed through the 10.4 and  $11.9 \mu\text{m}$  filters: equal flux values are found in both filters. Such a flux ratio,  $1 \pm 0.3$ , is consistent with either the HII region template or the AGN template if the  $9.7 \mu\text{m}$  silicate feature is not as deep as in the template.

#### 4. Active galactic nuclei: building the SED

This section focuses on the SED of the AGN in our sample. Historically, diagnostics of AGN SED were preferably applied to high luminosity objects, in order to avoid complication due

to the mixing of light from the AGN and from the host galaxy. Yet, the study of weaker close-by AGN is important since their proximity allows their inner structure to be unveiled down to physical scales of a few parsecs, corresponding to the expected sizes of some of their components. In such cases, the main difficulty arises from the fact that the contrast between the AGN and its host galaxy is low, particularly when the AGN is surrounded by regions of starburst activity. Then, large aperture photometric measurements can greatly differ from the actual AGN fluxes.

As the observational constraints on the torus models (Krolik & Begelman 1986; Pier & Krolik 1993; Granato & Danese 1994; Efstathiou & Rowan-Robinson 1995; Granato et al. 1997) come from the shape of the SED between 1 and  $20 \mu\text{m}$ , and from the depth of the  $9.7 \mu\text{m}$  silicate feature, it is particularly important to isolate the AGN and measure its flux free from contamination by other components. We provide a compilation of small aperture measurements of the NIR-MIR fluxes for our sample AGN (Table 3). The corresponding SED are shown in Fig. 8. In the top-left panel, along with the SED of Circinus, typical SED models have been overplotted for type 1 and type 2 AGN, as predicted using the radiative transfer code by Granato et al. (1997). Type 1 AGN show a flat SED (in  $\nu L_\nu$ ), while type 2 AGN show a SED with a steep fall off at NIR wavelengths.

- For Circinus, the compiled SED is from high resolution NACO NIR data and our MIR measurements. The SED is fully consistent with the ISO spectrum (overplotted) and

shows that the bulk of the NIR-MIR emission comes from a type 2 AGN.

- For NGC 1808, we plotted new NIR small aperture measurements (Galliano, in preparation) together with the TIMMI2 data. The MIR points are distributed similarly to those of Circinus, although slightly shifted towards lower luminosities. This supports the idea that the nucleus of NGC 1808 is indeed an AGN. However, at shorter wavelengths, the measurements show a SED increasing towards short wavelengths, suggesting the presence of a bright, stellar core. The overplotted large aperture ISO spectrum is from Siebenmorgen et al. (2001). Its flux level, about 10 times larger than that of the AGN, demonstrates that the central 1 kpc region is dominated by the emission from the starburst.
- The AGN in NGC 1365 is thought to be a type 2. Hence, its SED is expected to be decreasing from the MIR to the NIR. New small-aperture NIR measurements (Galliano, in preparation) are plotted together with the TIMMI2 fluxes and show that, in contrary to expectations, the SED is flat and consistent with that of a type 1 AGN. The presence of a local maximum at  $3.5 \mu\text{m}$  suggests a contribution from PAH. The AGN in NGC 1365 is thus a candidate for the detection of PAH around AGN.
- The NIR-MIR SED of NGC 2992 and NGC 7469 nuclei are respectively consistent with type 2 (steep SED) and type 1 (flat SED) AGN.

The remaining sources shown in Fig. 8 (NGC 5995, IZw1 and IIZw136) are described in Sect. 3.7. Detailed and unambiguous modelling of the SED of these AGN requires the use of additional data: as shown in Galliano et al. (2003) photometric measurements alone allow the fit of many different models of tori. A way to lift this degeneracy would be to use spatially resolved information, which means to observe these AGN with IR interferometers.

## 5. Circum-AGN environments: embedded star clusters in NGC 1808 and NGC 1365

MIR imaging at high spatial resolution provides the opportunity to detect young massive dust embedded clusters in starbursting galaxies. These clusters emit a bright IR continuum, infrared nebular emission lines and are strong cm radio sources. The IR continuum arises from the dust heated by stars in the cluster, while the lines and usually most of the cm continuum are produced by the HII regions surrounding the massive stars in the cluster and/or by supernova remnants (SNR).

To date, only a very limited number of such embedded clusters are known, namely the clusters in He2-10 (Kobulnicky & Johnson 1999; Beck et al. 2001; Vacca et al. 2002), NGC 5253 (Turner et al. 1998; Gorjian et al. 2001; Vanzi & Sauvage 2004), the Antennae (Mirabel et al. 1998; Gilbert et al. 2000), IIZw40 (Beck et al. 2002) and SBS0335-052 (Plante & Sauvage 2002). The embedded clusters are found to be young (a few Myr), massive ( $\sim 10^6 M_{\odot}$ ) and highly obscured ( $A_V = 5$  to 100).

The fact that the bright compact radio sources surrounding the AGN in NGC 1808 and NGC 1365 are found to be also intense MIR sources suggests that they are related to very dusty objects. Since these sources have no comparably intense optical counterpart (except NGC 1365/M 5), they are very likely to be embedded star clusters. Still, this interpretation needs quantitative support: in the following, we present comparisons between the predictions from a simple model for embedded star clusters and our observations in the MIR and the radio. We deliberately chose to consider a simple model, given the still limited amount of data available for comparison. The calculations in this section only intend to give support to the interpretation in terms of embedded clusters and to give rough estimates of their properties (order of magnitude for their age and mass). Detailed and more realistic modelling of such objects is postponed until new data, especially spectroscopic measurements, will become available. Throughout, the radio spectral indexes are noted  $\alpha$ , with  $S_{\nu} \propto \nu^{\alpha}$ .

### 5.1. Emission from young star clusters

Prior to being identified in the MIR, the radio sources surrounding the nuclei in NGC 1808 and NGC 1365 were commonly interpreted as radio supernovae or as supernova remnants (SNR). This was suggested by the negative values of their cm spectral indexes, indicating non-thermal emission (the radio measurements are given in Table 4). However, the interpretation in terms of isolated (i.e. not associated with a star cluster) radio supernova or SNR can now be discarded since these objects would not show up as IR sources for more than a few years (Weiler et al. 1986) and therefore would have a low probability of being detected as such. As we do detect them in the MIR, we consider instead that they are radio supernova or SNR associated with a young star cluster, where their probability of occurrence is large.

The observed radio spectral index for the sources range from steep to rather flat, but always indicate an important share of non-thermal processes. Two types of radio emission are expected from young compact clusters: free-free thermal emission from the HII regions surrounding the massive stars ( $\alpha \sim -0.1$  where  $\alpha$  can become positive in the case of optically thick emission), and non-thermal emission from both radio supernovae and SNR ( $\alpha \sim -0.9$ ). We examine hereafter the three possibilities. For simplification, we only consider optically thin emission, being conscious that such an assumption might not always hold true.

The first mechanism for the production of radio continuum is free-free emission in the HII regions surrounding massive stars. The observed flux depends on the rate of emission of H ionising photons ( $E \geq 13.6$  eV). Following Turner et al. (1998), in the case of optically thin radio emission, the cm flux is related to the number of ionising photons by the following relation:

$$\left(\frac{S_{\nu}}{\text{mJy}}\right)_{\text{HII}} = 1.45 \times 10^{-50} \left(\frac{d}{\text{Mpc}}\right)^{-2} \left(\frac{\nu}{\text{GHz}}\right)^{-0.1} \left(\frac{\dot{n}_{\text{N}}}{\text{s}^{-1}}\right), \quad (1)$$

**Table 4.** Measurements and predictions of the properties of the embedded star clusters in NGC 1808 and NGC 1365.

| Source name   | NGC 1808   |                     |                     |                     | NGC 1365            |                     |                     |
|---|------------|---------------------|---------------------|---------------------|---------------------|---------------------|---------------------|
|   | M2         | M3                  | M4                  | M8                  | M4                  | M5                  | M6                  |
| <sup>a</sup> Observed $\alpha_{3,6}^6$  | -0.92      | -0.28               | -0.40               | -0.61               | -0.39               | -0.77               | -0.44               |
| Estimated age (Myr)   | $\geq 6.3$ | $3.4^{+0.1}_{-0.1}$ | $3.5^{+0.5}_{-0.1}$ | $5.1^{+0.4}_{-1.0}$ | $3.5^{+0.5}_{-0.1}$ | $5.7^{+2.5}_{-0.3}$ | $3.8^{+0.7}_{-0.3}$ |
| <sup>a</sup> Observed 6 cm Lum [ $10^{25}$ erg s <sup>-1</sup> Hz <sup>-1</sup> ]                         | 9.2        | 15.2                | 14.6                | 14.6                | 110.5               | 58.6                | 113.4               |
| Predicted 6 cm Lum [ $10^{25}$ erg s <sup>-1</sup> Hz <sup>-1</sup> ]                                     | 9          | 57                  | 64                  | 41                  | 64                  | 37                  | 53                  |
| <sup>b</sup> Mass [ $10^6 M_{\odot}$ ]  | 1.6        | 0.3                 | 0.3                 | 0.4                 | 1.7                 | 1.6                 | 2.1                 |
| Observed 10.4 $\mu$ m Lum [ $10^{26}$ erg s <sup>-1</sup> Hz <sup>-1</sup> ]                              | $\leq 15$  | 15                  | $\leq 15$           | 20                  | $\leq 20$           | 250                 | 200                 |
| <sup>c</sup> Predicted 10.4 $\mu$ m Lum [ $10^{26}$ erg s <sup>-1</sup> Hz <sup>-1</sup> ] ( $T = 150$ K) | 10         | 60                  | 50                  | 40                  | 360                 | 170                 | 390                 |
| <sup>c</sup> Predicted 10.4 $\mu$ m Lum [ $10^{26}$ erg s <sup>-1</sup> Hz <sup>-1</sup> ] ( $T = 300$ K) | 50         | 370                 | 300                 | 270                 | 2300                | 1100                | 2500                |

<sup>a</sup> The radio measurements from Collison et al. (1994) for NGC 1808 and Sandqvist et al. (1995) for NGC 1365. The uncertainty on the spectral indexes is 0.1.

<sup>b</sup> Shifting the IMF lower mass cutoff to  $0.1 M_{\odot}$ , the mass would 2.5 times larger.

<sup>c</sup> The difference between observed and predicted luminosities at 10.4  $\mu$ m can be accounted for by absorption, the corresponding  $A_V$  values are discussed in Sect. 5.3.

where  $S_{\nu}$  is the flux density at frequency  $\nu$ ,  $\dot{n}_N$  is the rate of emission of ionising photons, and  $d$  is the distance to the source.

Some synchrotron sources appear and disappear within periods of months to years following type II or type Ib supernovae events and can be very intense. However, because of their short lifetime, and because we observe simultaneously several sources in NGC 1365 and NGC 1808, these radio supernovae are unlikely to be the dominant contributors. This contribution is therefore not included in the following discussion.

Finally, the radio emission from SNR starts about 50 years after the supernova event and persists for hundreds to thousands of years. We adopt the simple recipe given by Condon & Yin (1990), relating the non-thermal radio emission from galaxies to the type II supernova rate:

$$\left(\frac{S_{\nu}}{\text{mJy}}\right)_{\text{SNR}} = 10^6 \left(\frac{d}{\text{Mpc}}\right)^{-2} \left(\frac{\nu}{\text{GHz}}\right)^{\alpha} \left(\frac{\dot{n}_{\text{SN}}}{\text{yr}^{-1}}\right) \quad (2)$$

where  $S_{\nu}$  is the flux density at frequency  $\nu$ ,  $\alpha$  is the spectral index,  $d$  is the distance of the object and  $\dot{n}_{\text{SN}}$  is the supernova rate in yr<sup>-1</sup>. This mechanism is bound to play a role and will be considered in the discussion.

Let us evaluate the relative share of the two contributing mechanisms, free-free emission and non-thermal emission from SNR, along the evolution of a star cluster. As argued previously, the observed cm spectral indexes indicate that the emission has an important share of non-thermal emission produced by SNR. Using the stellar population evolutionary model Starburst99 developed by Leitherer et al. (1999), we can compute, for a given cluster, the time evolution of the supernova rate and of the emission rate of ionising photons. We choose a stellar population model with instantaneous star formation, solar metallicity, a total mass of  $10^6 M_{\odot}$  and a Salpeter initial mass function.

Instantaneous star formation is a straightforward assumption to model the star cluster evolution. Is solar metallicity a reasonable assumption? In spiral galaxies, heavy elements are

often found to be overabundant – with respect to solar – in the central region of the galaxy and also to exhibit an abundance gradient across the galaxy disc. In the case of NGC 1365, the oxygen abundance gradient (derived from the analysis of HII regions) is rather mild (0.02 dex/kpc) and gives an extrapolated oxygen abundance at the centre:  $12 + \log(\text{O}/\text{H}) = 9.1$  (Alloin et al. 1981). With a solar oxygen abundance of 8.66 in the same unit (Asplund et al. 2004), the metallicity at the centre of NGC 1365 is found to be around 3 times solar. The Starburst99 models presented in Leitherer et al. (1999) show that the number of ionising stars and the supernova rate depend very little on the metallicity at least between  $Z = 0.008$  and  $Z = 0.04$  (solar metallicity being  $Z = 0.02$ ). Hence, our assumption of solar metallicity for the clusters is well founded.

The lower and upper mass limits in the IMF are respectively set to 1 and  $100 M_{\odot}$ , and supernovae occur for star masses  $\geq 8 M_{\odot}$ . Figure 9 plots the Starburst99 predictions for the supernova rate (a) and emission rate of ionising photons (c). Figures 9b and d show the non-thermal 6 cm luminosity and the thermal 6 cm luminosity, computed using formulae (2) and (1), respectively. The considered mass for the cluster ( $10^6 M_{\odot}$ ) was chosen so as to predict radio luminosities which are of the order of those observed in the sources of NGC 1365 and NGC 1808 (see Table 4). Figures 9b and d show that after 3.5 Myr the non-thermal emission overcomes the thermal emission. This epoch depends mainly on the evolution of the thermal flux, which in turn depends on the slope of the IMF. For the chosen IMF, supernovae events stop at about  $\sim 35$  Myr after the birth of the cluster. The age of the radio sources in NGC 1808 and NGC 1365 should therefore lie between 3.5 and 35 Myr, given their fluxes and spectral indexes. How do the predicted cluster properties depend on the IMF cutoffs?

Decreasing the lower mass limit to  $0.1 M_{\odot}$  would neither affect the ionising flux of the cluster nor its supernovae rate, but the mass of the cluster would be larger by a factor 2.5. On the contrary, an increase of the upper mass limit of the IMF will have little effect on the cluster masses, but will significantly

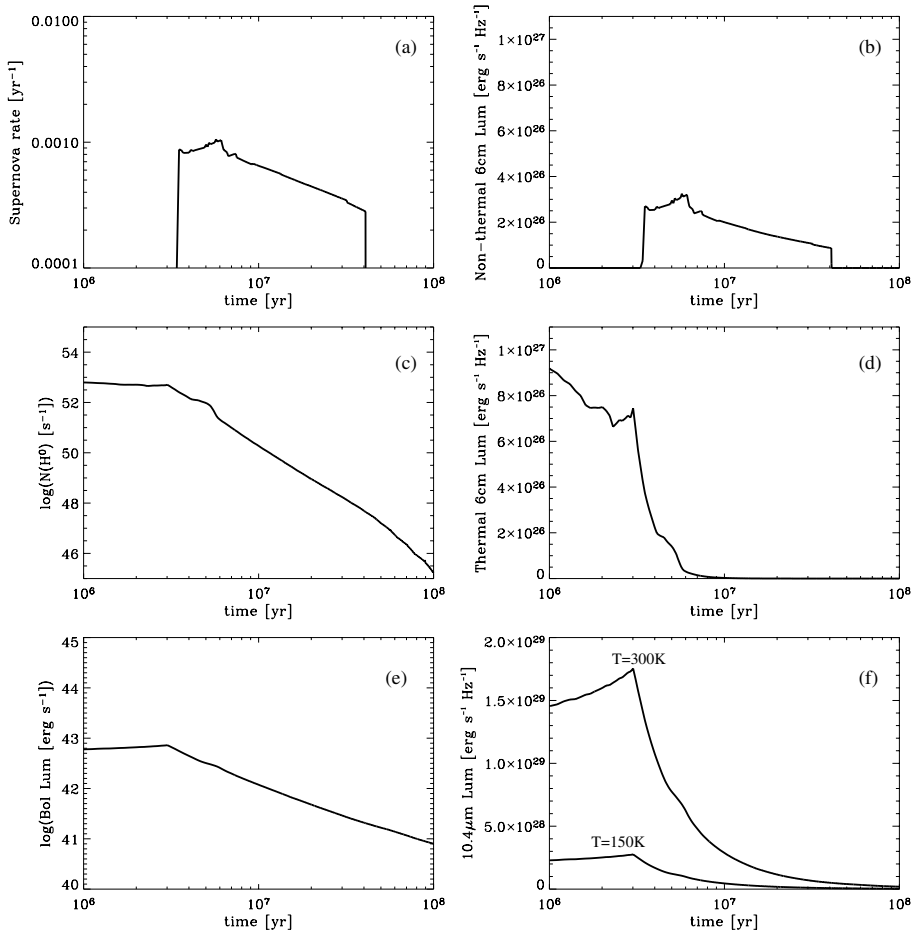


**Fig. 9.** Evolution of the properties of a star cluster. We consider a Starburst99 model for a  $10^6 M_{\odot}$  cluster with instantaneous star formation and Salpeter IMF. On the plots to the left, evolution of the star cluster intrinsic properties are shown. On the plots to the right, predicted observational properties as a function of time are shown. An index  $\alpha = -0.9$  is used for the SNR radio emission. **a)** Rate of supernova events per year. **b)** Non-thermal luminosity at 6 cm produced by the SNR. **c)** Lyman photon production rate. **d)** Thermal luminosity at 6 cm produced in the HII regions. **e)** Bolometric luminosity of the cluster. **f)** Evolution of the  $10.4 \mu\text{m}$  luminosity if all the energy of the stars is reprocessed in a black-body at respectively 300 K and 150 K.

increase the ionising luminosity of the cluster at very early stages (less than 3 Myr). Yet, even though the supernovae occur earlier, at these very early stages the cm emission remains dominated by the thermal emission. Hence, a higher upper mass limit for the IMF does not significantly affect the dating of the clusters. For the clusters in NGC 1808 and NGC 1365, the cm spectral indexes show that the clusters are at a later evolutionary stage, more than 3 Myr. Hence, a modification of the IMF upper mass would not greatly affect our conclusion. This is corroborated by a Starburst99 simulation, made with an upper mass cutoff of  $150 M_{\odot}$ .

The subsequent step is to check if the observed MIR fluxes are consistent with those expected from a star cluster embedded in dust. Precise modelling would require detailed radiative transfer calculations. However, as our aim is to perform a check at the level of the order of magnitude only, we can simplify the problem and represent the cluster emission as a black-body at a given temperature. As mentioned earlier, the continuum from VSG observed by ISO in starburst galaxies can be well fit by black bodies at  $T > 100$  K (Laurent 1999). We consider two values bracketing a plausible range of dust temperatures,

150 K and 300 K. Figure 9e plots the bolometric luminosity of the model cluster and Fig. 9f translates it into the luminosity at  $10.4 \mu\text{m}$  assuming that the whole energy is reprocessed in a black-body at 150 K (lower curve) and 300 K (upper curve). The  $10.4 \mu\text{m}$  luminosity for  $T = 300$  K is roughly one order of magnitude larger than for  $T = 150$  K, and in both cases larger than the observed  $10.4 \mu\text{m}$  luminosity (Table 4). This difference is discussed in Sect. 5.3.

Overall, the interpretation that the MIR/radio sources observed in the starbursting environments of NGC 1808 and NGC 1365 are embedded young massive star clusters is satisfactory.

## 5.2. Dating and weighing the clusters

Within the framework of the simple cluster modelling discussed above, it is possible to derive some quantitative parameters for each cluster. The index of the radio spectrum does not depend on the mass of the cluster whereas the supernova rate, Lyman photon emission rate and total luminosities are mass-scalable quantities. As illustrated in Fig. 10, an age can be

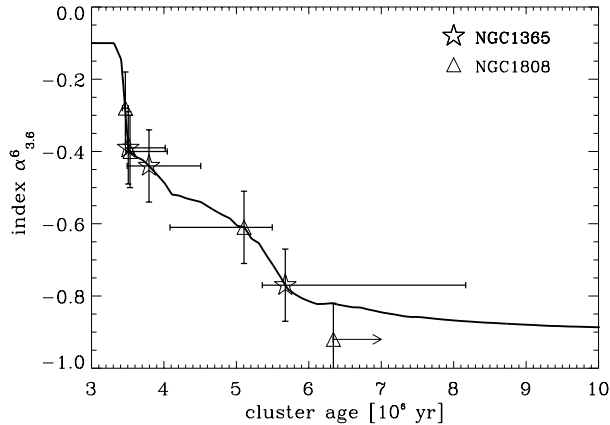


**Fig. 10.** The curve shows the evolution with time of the spectral index  $\alpha_{3.6}^6$  for our adopted cluster model (see Fig. 9 and corresponding description in Sect. 5.1). For a given model, an age may be attributed to every cluster in NGC 1808 and NGC 1365, depending only on the measured  $\alpha_{3.6}^6$  value.

attributed to the embedded clusters by comparing the observed  $\alpha$  value to the predicted one as the cluster evolves. Once an age is determined, we can compute the expected total 6 cm flux for the  $10^6 M_{\odot}$  cluster model. Rescaling this flux to the observed one provides the cluster mass. After mass and age have been derived for each cluster, it is possible to predict its  $10.4 \mu\text{m}$  flux if, as discussed above, we assume that the total luminosity from stars in the cluster is reemitted as a single black-body at temperature  $T$ . Results of these calculations are shown in Table 4.

The final figures we obtain are similar for all the bright clusters (except NGC 1808/M2). Their ages lie in the 3 to 6 Myr range. Even though their radio emission is not anymore dominated by the HII emission from massive stars, the clusters are very young. The masses inferred are between  $3 \times 10^5$  and  $2 \times 10^6 M_{\odot}$ , comparable to typical globular cluster masses.

### 5.3. Colour–colour diagrams

Modelling the MIR emission of the clusters with black-bodies was an easy and simple way to test this interpretation quantitatively. Yet, as shown with the MIR templates in Sect. 2.4, emission in the  $N$ -band is expected to be more complex, with the presence of the silicate feature at  $9.7 \mu\text{m}$ , PAH and emission lines ([SIV]  $10.4 \mu\text{m}$  and [NeII]  $12.8 \mu\text{m}$ ). The  $10.4 \mu\text{m}$  filter includes the silicate feature and coincides with the [SIV] line, the  $11.9 \mu\text{m}$  filter coincides with a strong PAH band, and finally the  $12.9 \mu\text{m}$  filter samples the continuum outside the silicate feature and coincides with the  $12.8 \mu\text{m}$  [NeII] line.

Figure 11 presents two colour–colour diagrams: to the left the  $11.9/12.9$  flux ratio vs. the  $10.4/11.9$  flux ratio and to the right the  $10.4/12.9$  flux ratio vs. the cm spectral index  $\alpha_{3.6}^6$ .

Let us discuss first the left diagram, comparing the  $N$ -band colours of the brightest MIR/radio sources in NGC 1808 and NGC 1365 (and the AGN of Circinus) with the  $N$ -band colours

of the template spectra of AGN, HII and PDR (Sect. 2.4). The filled symbols feature AGN while the open symbols are associated with the surrounding MIR/radio sources. On the colour–colour plot, the MIR/radio sources in NGC 1808 cover a narrow range of  $10.4/11.9$  flux ratios. On the contrary, the MIR/radio sources in NGC 1365 are spread in the  $10.4/11.9$  flux ratio and build up a sequence which is offset towards small  $11.9/12.9$  flux ratios. This offset could trace the uncertainty in the photometric calibration of the  $12.9 \mu\text{m}$  image due to local and unregistered variations of the sky transparency (see Sect. 2.3). New observations are needed to confirm the  $11.9/12.9$  flux ratios in NGC 1365. Even considering this uncertainty for NGC 1365, the MIR colours of the clusters in both galaxies are redder than the templates. This could result from the steepness of the continuum slope between 10 and  $14 \mu\text{m}$ , and/or from the presence of strong emission lines. A steep slope in this wavelength range can be produced by a deep  $9.7 \mu\text{m}$  silicate absorption feature. The colours of dust screened black-bodies at  $T = 150 \text{ K}$  and  $300 \text{ K}$  are overplotted in Fig. 11a. Since the  $10.4 \mu\text{m}$  filter samples the deepest part of the  $9.7 \mu\text{m}$  silicate feature and the  $12.9 \mu\text{m}$  filter samples its outer edge, a large amount of extinction (several tens of magnitudes in the  $V$ -band) is consistent with the small  $11.9/12.9$  and  $10.4/11.9$  flux ratios observed (deep silicate absorption). We are aware that a dust screen model is a coarse approximation when the MIR continuum is emitted by the dust itself. Yet, it is useful to compare the measured  $10.4 \mu\text{m}$  fluxes to those predicted by the model discussed in Sect. 5.2 and interpret the differences in terms of extinction by a dust screen. The  $A_V$  values derived this way range from a few magnitudes for  $T = 150 \text{ K}$  to several tens of magnitudes ( $\sim 50$ ) for  $T = 300 \text{ K}$ . PAH and/or [NeII]  $12.8 \mu\text{m}$  lines are also expected to contribute in producing the large observed ratios. Spectroscopic observations will be performed to investigate the silicate feature, the continuum slope and contribution of PAH and [NeII] lines.

Figure 11b provides the  $10.4/12.9$  flux ratio vs. the cm spectral index  $\alpha_{3.6}^6$ . As seen in the previous paragraph, the  $10.4/12.9$  flux ratio decreases as the silicate absorption feature gets deeper, or as the [NeII]  $12.8 \mu\text{m}$  line gets more intense. The plot suggests a possible correlation between the  $10.4/12.9$  flux ratio and the spectral index. As shown in Sect. 5.2, the spectral index is expected to decrease with time. Thus the  $x$ -axis of Fig. 11b may be regarded as a time indicator increasing from left to right. The increase of the  $10.4/12.9$  flux ratio together with that of the cm spectral index is broadly consistent with the picture of an evolving cluster, embedded in a cocoon of dust which dissipates with time. Along with the evolution of the cluster,

- (1) the ionising flux decreases as massive stars disappear through supernovae events, leading to a decrease of the [NeII]  $12.8 \mu\text{m}$  flux;
- (2) the dusty cocoon dissipates and consequently the dust column density decreases. This in turn translates into a weaker silicate absorption.

Both effects result in an increase of the  $10.4/12.9$  flux ratio with time.



- Forbes, D. A., Polehampton, E., Stevens, I. R., Brodie, J. P., & Ward, M. J. 2000, *MNRAS*, 312, 689
- Frogel, J. F., Elias, J. H., & Phillips, M. M. 1982, *ApJ*, 260, 70
- Galliano, E., Alloin, D., Granato, G. L., & Villar-Martín, M. 2003, *A&A*, 412, 615
- Genzel, R., Weitzel, L., Tacconi-Garman, L. E., et al. 1995, *ApJ*, 444, 129
- Gilbert, A. M., Graham, J. R., McLean, I. S., et al. 2000, *ApJ*, 533, L57
- Gorjian, V., Turner, J. L., & Beck, S. C. 2001, *ApJ*, 554, L29
- Gorjian, V., Werner, M. W., Jarrett, T. H., Cole, D. M., & Ressler, M. E. 2004, *ApJ*, 605, 156
- Granato, G. L., & Danese, L. 1994, *MNRAS*, 268, 235
- Granato, G. L., Danese, L., & Franceschini, A. 1997, *ApJ*, 486, 147
- Hunt, L. K., Malkan, M. A., Rush, B., et al. 1999, *ApJS*, 125, 349
- Junkes, N., Zinnecker, H., Hensler, G., Dahlem, M., & Pietsch, W. 1995, *A&A*, 294, 8
- Kalas, P., & Wynn-Williams, C. G. 1994, *ApJ*, 434, 546
- Keto, E., Ball, R., Arens, J., et al. 1993, *ApJ*, 413, L23
- Keto, E., Hora, J. L., Fazio, G. G., Hoffmann, W., & Deutsch, L. 1999, *ApJ*, 518, 183
- Kobulnicky, H. A., & Johnson, K. E. 1999, *ApJ*, 527, 154
- Koribalski, B., Dettmar, R.-J., Mebold, U., & Wielebinski, R. 1996, *A&A*, 315, 71
- Krabbe, A., Böker, T., & Maiolino, R. 2001, *ApJ*, 557, 626
- Kristen, H., Jorsater, S., Lindblad, P. O., & Bokseberg, A. 1997, *A&A*, 328, 483
- Krolik, J. H., & Begelman, M. C. 1986, *ApJ*, 308, L55
- Laurent, O. 1999, Ph.D. Thesis
- Laurent, O., Mirabel, I. F., Charmandaris, V., et al. 2000, *A&A*, 359, 887
- Léger, A., & Puget, J. L. 1984, *A&A*, 137, L5
- Leitherer, C., Schaerer, D., Goldader, J. D., et al. 1999, *ApJS*, 123, 3
- Lindblad, P. O. 1999, *A&A Rev.*, 9, 221
- Marco, O., & Alloin, D. 1998, *A&A*, 336, 823
- Matt, G., Guainazzi, M., Maiolino, R., et al. 1999, *A&A*, 341, L39
- Mauder, W., Weigelt, G., Appenzeller, I., & Wagner, S. J. 1994, *A&A*, 285, 44
- Mazzarella, J. M., Voit, G. M., Soifer, B. T., et al. 1994, *AJ*, 107, 1274
- Miles, J. W., Houck, J. R., & Hayward, T. L. 1994, *ApJ*, 425, L37
- Mirabel, I. F., Vigroux, L., Charmandaris, V., et al. 1998, *A&A*, 333, L1
- Mizutani, K., Suto, H., & Maihara, T. 1994, *ApJ*, 421, 475
- Moorwood, A., Cuby, J.-G., Biereichel, P., et al. 1998, *The Messenger*, 94, 7
- Morgan, W. W. 1958, *PASP*, 70, 364
- Moshir, M., et al. 1990, in *IRAS Faint Source Catalogue*, version 2.0
- Murtagh, F., & Starck, J.-L. 1999, *Amer. Astron. Soc. Meet.*, 194, 0
- Pier, E. A., & Krolik, J. H. 1993, *ApJ*, 418, 673
- Pina, R. K., Jones, B., Puetter, R. C., & Stein, W. A. 1992, *ApJ*, 401, L75
- Plante, S., & Sauvage, M. 2002, *AJ*, 124, 1995
- Prieto, A., Meisenheimer, K., Marco, O., et al. 2004 [[arXiv:astro-ph/0406620](https://arxiv.org/abs/astro-ph/0406620)]
- Rieke, G. H. 1978, *ApJ*, 226, 550
- Roche, P. F., Aitken, D. K., Smith, C. H., & Ward, M. J. 1991, *MNRAS*, 248, 606
- Sérsic, J. L., & Pastoriza, M. 1965, *PASP*, 77, 287
- Saikia, D. J., Pedlar, A., Unger, S. W., & Axon, D. J. 1994, *MNRAS*, 270, 46
- Saikia, D. J., Unger, S. W., Pedlar, A., et al. 1990, *MNRAS*, 245, 397
- Sams, B. J., Genzel, R., Eckart, A., Tacconi-Garman, L., & Hofmann, R. 1994, *ApJ*, 430, L33
- Sandage, A., & Tammann, G. A. 1981, *A revised Shapley-Ames Catalog of bright galaxies* (Washington: Carnegie Institution, Preliminary version)
- Sandqvist, A., Joersaeter, S., & Lindblad, P. O. 1995, *A&A*, 295, 585
- Sandqvist, A., Jorsater, S., & Lindblad, P. O. 1982, *A&A*, 110, 336
- Schinnerer, E., Eckart, A., & Tacconi, L. J. 1998, *ApJ*, 500, 147
- Siebenmorgen, R., Moorwood, A., Freudling, W., & Kaeuff, H. U. 1997, *A&A*, 325, 450
- Siebenmorgen, R., Krügel, E., & Laureijs, R. J. 2001, *A&A*, 377, 735
- Sturm, E., Lutz, D., Tran, D., et al. 2000, *A&A*, 358, 481
- Tacconi-Garman, L. E., Sternberg, A., & Eckart, A. 1996, *AJ*, 112, 918
- Tansley, D., Birkinshaw, M., Hardcastle, M. J., & Worrall, D. M. 2000, *MNRAS*, 317, 623
- Tomono, D., Doi, Y., Usuda, T., & Nishimura, T. 2001, *ApJ*, 557, 637
- Turner, J. L., & Ho, P. T. P. 1985, *ApJ*, 299, L77
- Turner, J. L., Ho, P. T. P., & Beck, S. C. 1998, *AJ*, 116, 1212
- Ulvestad, J. S., & Antonucci, R. R. J. 1997, *ApJ*, 488, 621
- Ulvestad, J. S., Wilson, A. S., & Sramek, R. A. 1981, *ApJ*, 247, 419
- Vacca, W. D., Johnson, K. E., & Conti, P. S. 2002, *AJ*, 123, 772
- Vanzi, L., & Sauvage, M. 2004, *A&A*, 415, 509
- Véron, P., Lindblad, P. O., Zuiderwijk, E. J., Véron, M. P., & Adam, G. 1980, *A&A*, 87, 245
- Véron-Cetty, M.-P., & Véron, P. 1985, *A&A*, 145, 425
- Ward, M., Elvis, M., Fabbiano, G., et al. 1987, *ApJ*, 315, 74
- Weiler, K. W., Sramek, R. A., Panagia, N., van der Hulst, J. M., & Salvati, M. 1986, *ApJ*, 301, 790
- Wilson, A. S., Helfer, T. T., Haniff, C. A., & Ward, M. J. 1991, *ApJ*, 381, 79